[UCI]I804:24011-200000360035

2021년 2월

석사학위 논문

Lithium—oxygen batteries with multi-layered lithium-ion conducting solid electrolytes

조선대학교 대학원

첨단소재공학과

최 영 빈

Lithium—oxygen batteries with multi-layered lithium-ion conducting solid electrolytes

다층구조 리튬이온 전도성 고체전해질을 적용한 리튬-산소 전지 개발

2021년 02월 25일

조선대학교 대학원

첨단소재공학과

최 영 빈

Lithium—oxygen batteries with multi-layered lithium-ion conducting solid electrolytes

지도교수 강 현 철

이 논문을 공학 석사학위신청 논문으로 제출함

2020년 10월

조선대학교 대학원

첨단소재공학과

최 영 빈

최영빈의 석사학위논문을 인준함

위원장 조선대학교 교수 이종국 (인)
위 원 조선대학교 교수 신동찬 (인)
위 원 조선대학교 교수 강현철 (인)

2020년 11월

조선대학교 대학원

Table of Contents

List of Tables

List of Figures

ABSTRACT

Lithium—oxygen batteries with multi-layered lithium-ion conducting solid electrolytes

Youngbin Choi
Advisor : Prof. Hyun-Chul Kang
Dept. of Advanced Materials Engineering
Graduate School of Chosun University

With the increasing demand in electric vehicles, rechargeable Li—O_2 batteries (LOBs) are attracting considerable attention, as their theoretical energy density is several times higher than that of current Li—ion batteries. To date, ether-based organic liquid electrolytes have been commonly used for LOBs, but unfortunately, they are unstable against superoxide radicals generated during LOB operation. In this respect, other candidates based on sulfones, sulfoxides, and ionic liquids have been explored as alternative electrolytes for LOBs. A truly stable electrolyte is yet to be demonstrated, however. The use of solid-state, Li^+-selective conducting membranes (LSSMs) in LOBs may provide an effective approach to address the problems associated with the organic electrolytes. Furthermore, an LSSM with relatively high mechanical robustness can retain the dendrite growth on the Li metal anode during repeated discharge-charge cycling and can protect the Li metal anode from parasitic reactions with the impurity species.

Herein, we propose a solid-state LOB design based on a mutli-layered LSSM structure. A $Li_{1+x+y}Al_xTi_{2-x}Si_yP_{3-y}O_{12}$ (LATP) based LSSM with a multi-layered (dense/porous) structure is prepared via a tape-casting process combined with co-sintering. A porous LATP layer is then deposited with carbon nanotubes (CNTs) serving as the cathode. The electrochemical performance of the constructed solid-state LOBs is characterized and the efficacy of the LSSM-based LOB design is discussed.

국문요지

다층구조 리튬이온 전도성 고체전해질을 적용한 리튬—산소 전지 개발

Youngbin Choi
Advisor : Prof. Hyun-Chul Kang
Dept. of Advanced Materials Engineering
Graduate School of Chosun University

전기자동차의 수요가 증가함에 따라 재충전 리튬—산소 전지 (Li—O_2 battery) 는 현재 사용되는 리튬—이온 배터리보다 몇 배 더 높은 이론 에너지 밀도를 가지고 있어 상당한 관심을 받고 있습니다. 현재까지 에테르 기반 유기 액체 전해질은 리튬-산소 전지에 일반적으로 사용되지만 안타깝게도 리튬—산소 전지의 작동 중에 생성되는 슈퍼 옥사이드 라디칼에 대해서 불안정합니다. 이와 관련하여 설폰, 설폭사이드 및 이온성 액체를 기반으로 하는 다른 후보들이 리튬—산소 전지의 대체 전해질로 연구가 진행되었습니다. 그러나 안정성이 우수한 전해질은 아직 입증되지 않았습니다. 리튬-산소 전지에서 고체 상태의 리튬 이온 전도성 막을 사용하면 유기 전해질과 관련된 문제를 해결하는 효과적인 접근 방식을 제공할 수 있습니다. 또한, 상대적으로 높은 기계적 견고성을 가진 리튬 이온 전도성 막은 반복적인 방전-충전 사이클링 동안 리튬 금속 양극에서 수상 돌기 성장을 제어할 수 있으며 불순물과 리튬 금속 음극 사이에서의 부반응을 보호할 수 있습니다.

여기서 우리는 다층구조의 리튬 이온 전도성 막을 기반으로 한 고체 상태 리튬-산소 전지의 디자인을 제안합니다. 다층 (고밀도 층/다공성 층) 구조의 $Li_{1+x+y}Al_xTi_{2-x}Si_yP_{3-y}O_{12}$ (LATP) 를 기반으로 한 리튬 이온 전도성 막은 공-소결과 테이프 캐스팅 공정을 통해 제작됩니다. 다공성 층은 양극 역할을 하는 탄소 나노 튜브 (CNTs) 로 증착되어 있습니다. 구성된 고체 상태 리튬—산소 전지의 전기화학 성능을 특성화하고 리튬 이온 전도성 막을 기반으로 한 리튬—산소 전지 설계의 효율성에 대해 연구합니다.

Ⅰ. Introduction

Eco-friendly energy conversion and storage systems with high energy density are required for the sustainable development of human society. Lithium—oxygen batteries (LOBs), which consist of an energy density several times higher than that of the current lithium-ion batteries, are receiving considerable attention [1-4]. They can have a high theoretical energy density owing to the formation and decomposition of the discharge product (Li_2O_2). Further, they generally utilize a Li metal anode, a porous separator with a Li-ion conducting liquid electrolyte, a porous carbon cathode, and are exposed to ambient air or O_2 [1,2,5,6]. Significant progress has been made with the use of organic liquid electrolytes, but various technical challenges remain, such as low energy efficiency and a poor life cycle life. First, the use of liquid electrolytes causes a rare evaporation, leakage, flammability, low oxygen solubility, and chemical instability [7 - 12]. Second, a corrosion of lithium metal occurs when air is used as a source of LOB and an irreversible reaction occurs at the cathode side [13,14]. Recent studies have suggested the use of non-porous, solid-state Li-ion-selective conducting membranes with the following advantages as an effective solution to this problem [15,16]. First, Li-ion-selective conducting membranes (LSSMs) can suppress dendrites occurring in the lithium metal anode with relatively high mechanical robustness. Second, they prevent side reactions from reactants (O_2) and impurity species (e.g., H_2O and CO_2) that diffuse from the cathode [11,12]. Third, there is an increasing stability because volatile organic electrolytes are not used. Finally, various battery designs and configurations are possible [17,18].

$Li_{1.3}Al_{0.3}Ti_{1.7}(PO_4)_3$ (LATP) based on a NASICON-type solid membrane is particularly intriguing because it has better stability in moisture [19,20] and a higher ionic conductivity at room temperature (298 K) compared to other solid-state electrolytes (SSEs) (> 1.0×10^{-4} S cm-1) [21-24]. Visco et al. [25] proposed a lithium - air cell by the stability in air and water with an LSSM based on the NASICON-type $Li_3M_2(PO_4)_3$. In addition, Kwak et al. reported the composition and electrochemical testing of LOB cells wherein the anode electrode and negative electrode compartments were physically separated by LSSMs [16]. Zhou et al. proposed a lithium–air battery composed of a lithium–ion-conductive solid electrolyte that achieved a discharge capacity of 950 mAh g_{carbon}^{-1} at a high current density (100 mA g_{carbon}^{-1}) [26]. Results of the LOB cells presented an improved electrochemical performance in terms of cycling stability and efficiency compared to that of LOBs using conventional liquid electrolytes. However, in most previous studies [15,16,17], it was assembled into thick LSSM pellets to maintain sufficient mechanical strength for cell assembly. Meanwhile, solid-state lithium batteries have high resistance and limited three-phase boundaries (TPBs) due to solid–solid contact.

To address this problem, we proposed a new LSSM structure through a tape casting process to minimize the thickness of the membranes without sacrificing the mechanical properties based on LATP [27,28]. A thin powder sheet is formed through slurry coating to form a porous layer that acts as a structural support through co-sintering at high temperatures, and a thin dense layer to rapidly transport lithium ions. Unlike existing liquid electrolytes, multi-layered LSSMs presented a more stable electrochemical performance. Based on LSSMs, a new design was developed to address the problem of interfacial contact between the electrolyte and the electrode. CNTs were directly grown on the porous layer, which served as a structural support as the cathodic side, thereby providing an easier lithium-ion transport path and an additional space suitable for accommodating discharge products. In addition, we could expect the electrochemical performance of a lithium—oxygen battery that does not use an electrolyte on the cathode side and has a more stable and long cycle life.

A. Lithium secondary battery

With the development of advanced technology, lithium batteries have gained popularity in different fields, such as various information and communication devices and electric vehicles. Lithium secondary batteries, which have been commercialized since the early 1990s, have been extensively investigated, but they remain to have a high energy density, high operating voltage, and a long cycle life performance, resulting in increasing demands. In addition, these batteries have exceptional properties that meet the high density and high efficiency performance. Figure 1 shows the operating principle and components of a lithium secondary battery. A lithium secondary battery is mainly composed of a positive electrode material, separator, liquid electrolyte, and negative electrode material that must have a structure that is easy to intercalate and deintercalate when repeated cycles are performed to achieve excellent properties.

Lithium ions move rapidly toward the electrode through the electrolyte, and a reaction occurs through the current collector to the electrode. In addition, the amount of ions intercalated into the electrode determines the amount of energy that can be stored. In other words, the movement speed of lithium ions is determined by the electrolyte and electrode and has a significant influence. Lithium has the lowest standard reduction potential and is one of the most widely known metals in nature. When applied to batteries, the energy density is significantly high. Lithium—ion secondary batteries have a high operating voltage; therefore, an organic solvent must be used, rather than aqueous electrolyte. A material with a lattice structure is mainly used as an electrode, which facilitates the intercalation and deintercalation of lithium ions. Lithium is one of the most common metals in nature and has the lowest standard reduction potential, resulting in a high electromotive force of 3 V or higher. When applied as an electrode material, lithium has a high energy density per weight and volume.

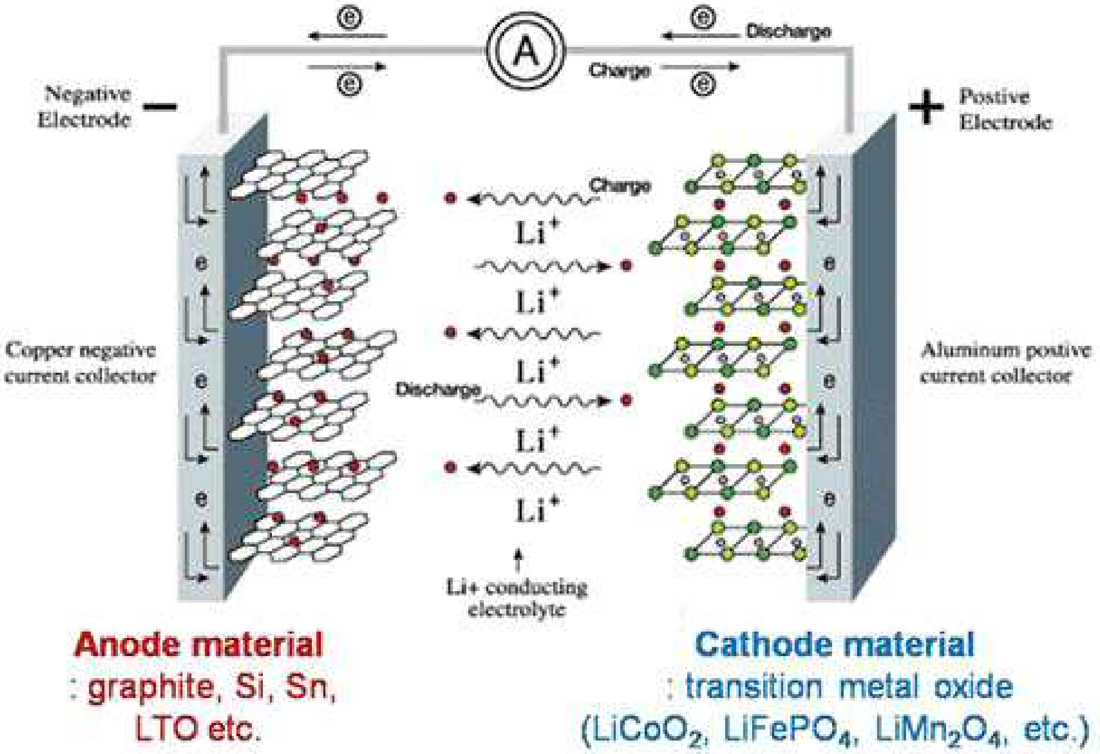

Figure 1. Schematic of the structure and operating of the Lithium secondary battery [29].

B. Lithium—oxygen rechargeable battery

Rechargeable LOBs use atmospheric oxygen as the cathode. Therefore, it has the advantage of being lightweight because it does not require a cathode material except for the current collector [30]. It has a significantly high theoretical energy density close to that of a battery powered by gasoline and was proposed by Abraham in 1996s [31]. Figure 2 presents the energy densities of various rechargeable batteries. Rechargeable lithium—oxygen batteries work by the following chemical reactions [32]:

$$2Li + O_2 \leftrightarrow Li_2O_2 \ (3.10V) \tag{1-1}$$

$$Li + \frac{1}{2}O_2 \leftrightarrow LiO_2 \ (2.91V) \tag{1-2}$$

During the discharging process, lithium ions move from the lithium metal anode through the electrolyte to the cathode and form a discharge product through a chemical reaction with oxygen on the cathode side, as expressed in Eqs. 1-1 and 1-2. The chemical reaction between lithium ions and oxygen produces lithium oxide and is converted into energy. The charging process is separated into lithium and oxygen by applying voltage to the lithium oxide in reverse order of the discharging process. Figure 3 illustrates the working principle and structure of a rechargeable LOB [31].

LOBs have several advantages over lithium—ion batteries, such as a significantly high theoretical energy density and low cost. However, their commercialization has been constrained by many technicalities. Compared to the reported theoretical energy density, present LOBs exhibit a significantly lower energy density, and unwanted reactions occur due to the use of air, resulting in low cycle performance and energy efficiency [31-35]. The energy efficiency of the LOB must be 90% or higher for commercialization and must present a high density close to the theoretical energy density.

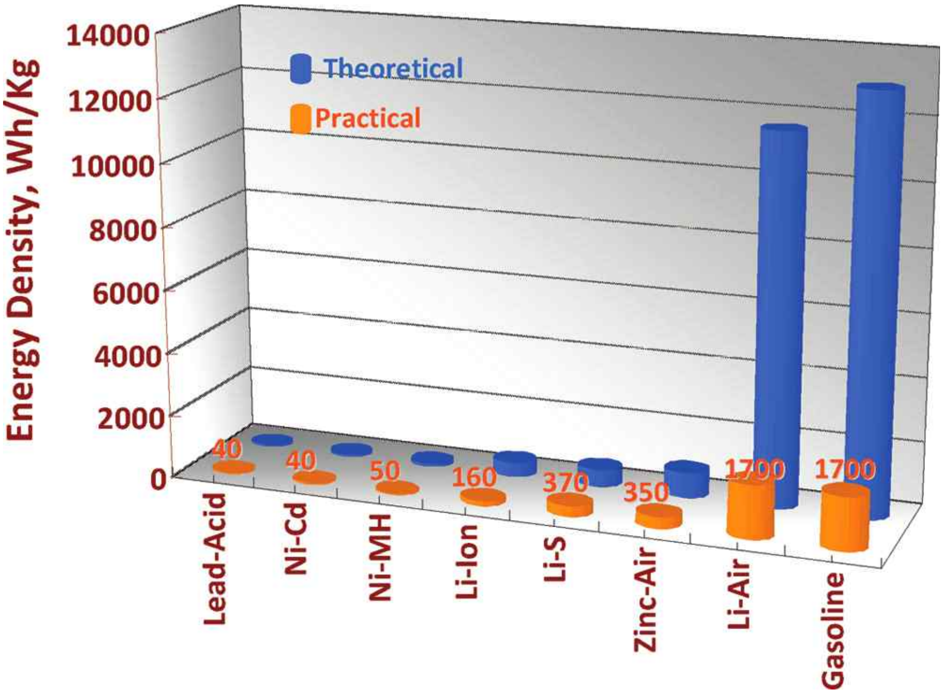

Figure 2. The energy densities for different types of rechargeable batteries [31].

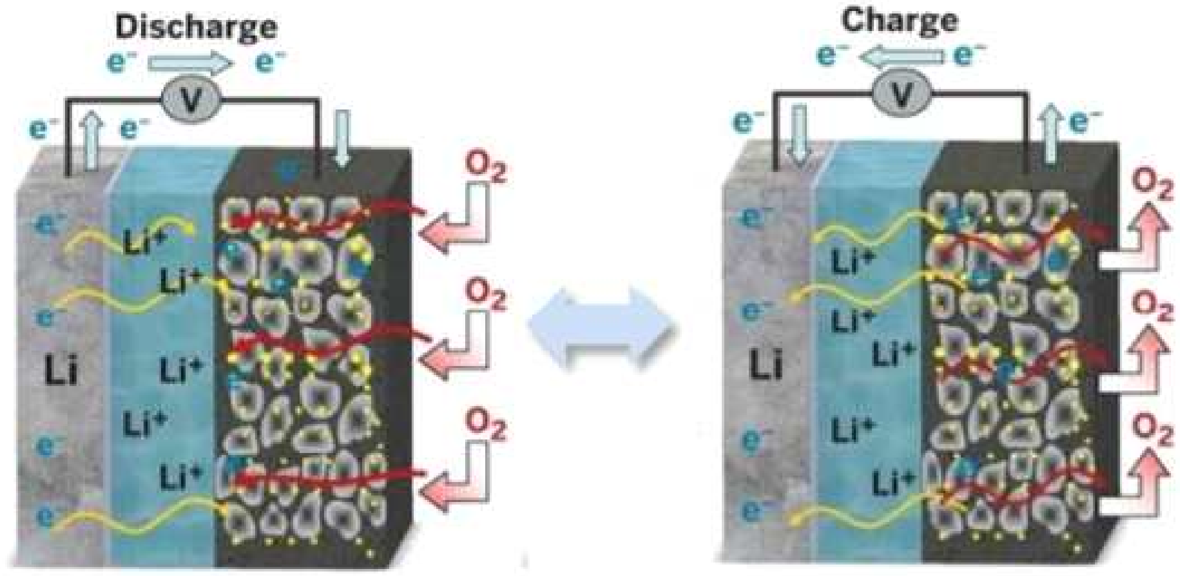

Figure 3. The operating principle of rechargeable lithium—oxygen battery [31].

C. Solid-state lithium battery

Liquid electrolytes have been mainly used in lithium—ion batteries owing to their high ionic conductivity and sufficient contact with electrodes. However, they are physically and chemically unstable owing to potential leaks and a relatively high electrical conductivity. In addition, due to flammability, there are concerns of explosions or fires, and chemical stability emerges [29,36].

To address this problem, a study was conducted on a solid electrolyte that is stable and significantly safer for lithium ions with minimal electronic conductivity. Solid electrolytes offer the possibility of using Li metal anodes to increase cell voltage and capacity [37,38] or to use liquid cathodes with higher capacities, compared to solid insert cathodes [39]. Figure 4 [40] and Table 1 present the comparison of the properties of solid and liquid electrolytes. Specifically, batteries with solid electrolytes reduce the power density owing to their relatively low ionic conductivity compared to liquid electrolytes. Therefore, research has focused mainly on electrolytes with high lithium ion conductivity. Materials that exhibit high ionic conductivity ($\sim 10^{-3}$ to 10^{-4} S cm^{-1}) at room temperature (298 K) were found to be $Li_{0.5}La_{0.5}TiO_3$ [41, $Li_{10}GeP_2S_{12}$ [42], and $LiTi_2(PO_4)_3$ [43].

Combined with semiconductor process technology to control nano-sized materials, thin-film lithium batteries offer various design directions with potentially high energy densities. They can be used in applications that require high power density, such as wireless sensors or smart cards. They can be classified into a thin film type and a thick film type (bulk type) according to the manufacturing method and type of solid electrolyte. The former, which is a thin-film type all-solid-state lithium secondary battery, is commonly manufactured via a dry process in a vacuum state, such as deposition of a LiPON-based solid electrolyte. The latter, which is a thick-film type all-solid-state lithium secondary battery, is manufactured by heating and pressing inorganic solid electrolyte particles, such as oxides or sulfides to prepare a solid electrolyte in the form of a sheet or pellet, and then inserting it between the existing electrodes. The concept of a thin-film all-solid-state lithium secondary battery is basically the same as lithium—ion batteries by repetitive charging and discharging by intercalation and/or deintercalation reaction at the positive electrode, striping and/or plating reaction at the lithium negative electrode, and lithium ions in the solid electrolyte. It is transmitted by a type of hopping effect. Solid electrolytes are not only the significant feature of thin-film all-solid-state lithium secondary batteries, but also all current collectors to the electrodes are manufactured through vacuum dry processes, such as PVD (Physical Vapor Deposition) or CVD (Chemical Vapor Deposition). However, thin-film all-solid-state lithium secondary batteries have various advantages, such as long cycle life, high energy density, high power, high-speed charging, and safety, but they have a limited capacity. However, owing to the characteristics of the thin-film type, there are significant limitations in increasing the area or the thickness of the electrode layer from a performance perspective. In addition, when the thickness of the LiPON electrolyte is increased, a rapid deterioration in performance occurs. Recently, the characteristics of a ceramic solid electrolyte comprising a thick film have been reported in which the ionic conductivity was close to 10^{-3} $S \cdot cm^{-1}$ at room temperature [44]. In particular, in the case of sulfide systems, properties approaching 10^{-2} S cm^{-1} have also been recently reported. Early ceramic-based solid electrolytes have problems, such as the significant thickness of the formed electrolyte and low ionic conduction characteristics. Therefore, when applied to a lithium secondary battery, the output performance rapidly deteriorates. However, it is expected that the problem of deteriorating the output performance will not be discussed further as the ionic conductivity is close to that of the liquid electrolyte. As previously indicated, unlike thin-film lithium secondary batteries wherein the current collector-electrode electrolyte is sequentially manufactured in a batch process, the thick-film type all-solid-state lithium secondary battery is manufactured via the assembly process and is similar to the existing lithium secondary battery.

Table 1. A comparison of various electrolyte systems for commercial Li—ion batteries [45].

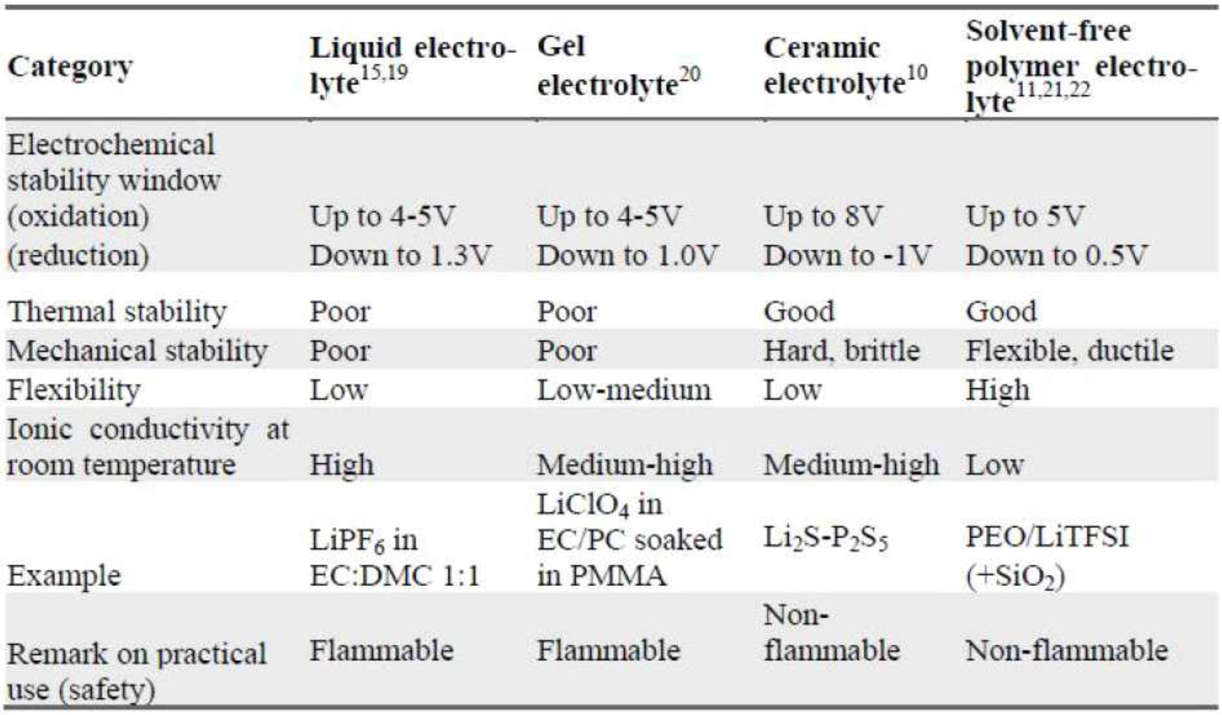

Category	**Liquid electrolyte^{15,19}**	**Gel electrolyte^{20}**	**Ceramic electrolyte^{10}**	**Solvent-free polymer electrolyte^{11,21,22}**
Electrochemical stability window (oxidation) (reduction)	Up to 4-5V Down to 1.3V	Up to 4-5V Down to 1.0V	Up to 8V Down to -1V	Up to 5V Down to 0.5V
Thermal stability	Poor	Poor	Good	Good
Mechanical stability	Poor	Poor	Hard, brittle	Flexible, ductile
Flexibility	Low	Low-medium	Low	High
Ionic conductivity at room temperature	High	Medium-high	Medium-high	Low
Example	$LiPF_6$ in EC:DMC 1:1	$LiClO_4$ in EC/PC soaked in PMMA	Li_2S-P_2S_5	PEO/LiTFSI ($+SiO_2$)
Remark on practical use (safety)	Flammable	Flammable	Non-flammable	Non-flammable

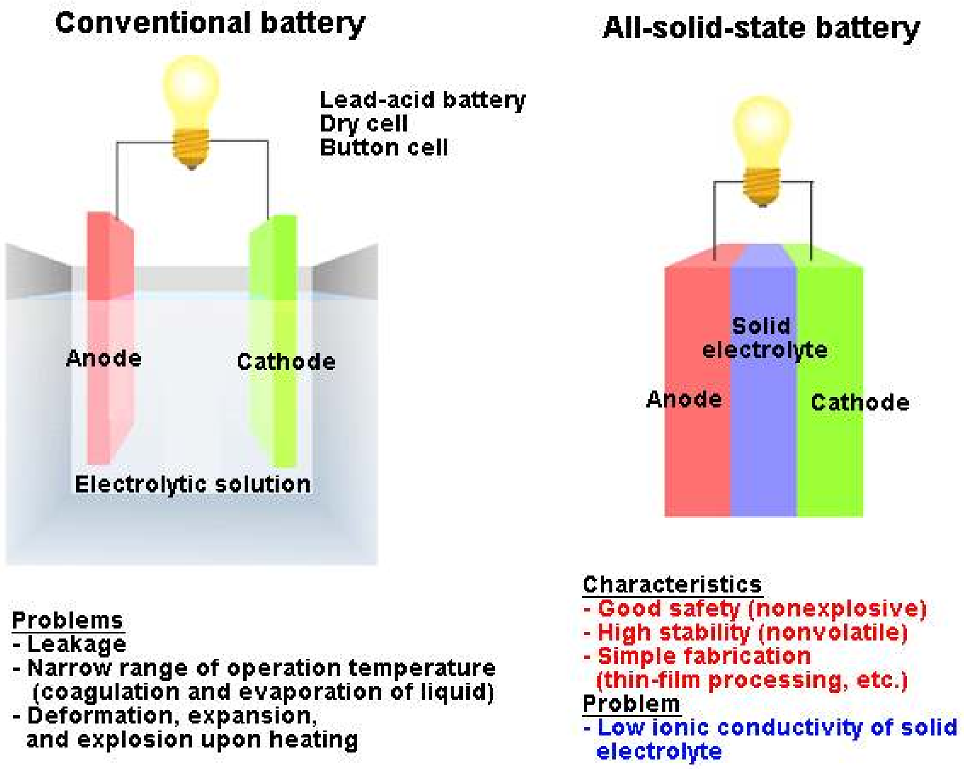

Figure 4. Compared of the characteristics of a solid and liquid electrolyte [40].

Reference

[1] J. Lu, L. Li, J.-B. Park, Y.-K. Sun, F. Wu and K. Amine, *Chem. Rev.*, 2014, **114**, 5611.

[2] K.-N. Jung, J. Kim, Y. Yamauchi, M.-S. Park, J.-W. Lee and J.H. Kim, *J. Mater. Chem. A*, 2016, **4**, 14050.

[3] S. Chu, Y. Cui, N. Liu, The path towards sustainable energy, *Nat. Mater.*, 2016, **16**, 16-22.

[4] J.H. Montoya, L.C. Seitz, P. Chakthranont, A. Vojvodic, T.F. Jaramillo, J.K. Nørskov, *Nat. Mater.*, 2017, **16**, 70-81.

[5] D. Aurbach, B.D. McCloskey, L.F. Nazar and P.G. Bruce, *Nat. Energy*, 2016, **1**, 16128.

[6] Z. Lyu, Y. Zhou, W. Dai, X. Cui, M. Lai, L. Wang, F. Huo, W. Huang, Z. Hu and W. Chen, *Chem. Soc. Rev.*, 2017, **46**, 6046.

[7] G. Girishkumar, B. D. McCloskey, A. C. Luntz, S. Swanson and W. Wilcke, *J. Phys. Chem. Lett.*, 2010, **1**, 2193 – 2203.

[8] C. O. Laoire, S. Mukerjee, K. Abraham, E. J. Plichta and M. A. Hendrickson, J. *Phys. Chem. C.*, 2011, **114**, 9178 – 9186.

[9] B. Scrosati and J. Garche, *J. Power Sources.*, 2010, **195**, 2419 – 2430.

[10] Z. Peng, S. A. Freunberger, Y. Chen and P. G. Bruce, *Science.*, 2012, **337**, 563 – 566.

[11] B. McCloskey, D. Bethune, R. Shelby, G. Girishkumar and A. Luntz, *J. Phys. Chem. Lett.*, 2011, **2**, 1161 – 1166.

[12] J. J. Xu, D. Xu, Z. L. Wang, H. G. Wang, L. L. Zhang and X. B. Zhang, *Angew. Chem., Int. Ed.*, 2013, **52**, 3887 – 3890.

[13] J.L. Shui, J.S. Okasinski, P. Kenesei, H.A. Dobbs, D. Zhao, J.D. Almer, D.J. Liu, *Nat. Commun.*, 2013, **4**, 2255.

[14] X. Shen, H. Liu, X.-B. Cheng, C. Yan, J.Q. Huang, *Energy Storage Mater.*, 2018, **12**, 161 – 175.

[15] B.J. Bergner, M.R. Busche, R. Pinedo, B.z.B. Berkes, D. Schröder and J.r. Janek, *ACS Appl. Mater. Interfaces*, 2016, **8**, 7756.

[16] W.J. Kwak, H.G. Jung, D. Aurbach and Y.K. Sun, *Adv. Energy Mater.*, 2017, **7**, 1701232.

[17] K.-N. Jung, J.-H. Jung, W.B. Im, S. Yoon, K.-H. Shin and J.-W. Lee, *ACS Appl. Mater. Interfaces*, 2013, **5**, 9902.

[18] P. He, T. Zhang, J. Jiang and H. Zhou, *J. Phys. Chem. Lett.*, 2016, **7**, 1267.

[19] X. B. Zhu, T. S. Zhao, Z. H. Wei, P. Tan and L. An, *Energy Environ. Sci.*, 2015, **8**, 3745-3754.

[20] M. Balaish, A. Kraytsberg and Y. Ein-Eli, *Phys. Chem. Chem. Phys.*, 2014, **16**, 2801-2822.

[21] L. Hallopeau, D. Bregiroux, G. Rousse, D. Portehault, P. Stevens, G. Toussaint and C. Laberty-Robert, *J. Power Sources.*, 2018, **378**, 48-52.

[22] A. Rosenberger, Y. Gao and L. Stanciu, *Solid State Ionics*, 2015, **278**, 217-221.

[23] S. Duluard, A. Paillassa, L. Puech, P. Vinatier, V. Turq, P. Rozier, P. Lenormand, P.-L. Taberna, P. Simon and F. Ansart, *J. Eur. Ceram. Soc.*, 2013, **33**, 1145-1153.

[24] H. Bai, J. Hu, X. Li, Y. Duan, F. Shao, T. Kozawa, M. Naito and J. Zhang, *Ceram. Int.*, 2018, **44**, 6558-6563.

[25] S. J.Visco, E.Nimon, B.Katz, L. C. D.Jonghe and M. Y.Chu, Abstract 0389, *The 210th Electrochemical Society Meeting Abstracts, Cancun, Mexico*, 2006, **Vol. 2006-2**.

[26] Y. Wang and H. Zhou, *Energy Environ. Sci.*, 2011, **4**, 1704- 1707.

[27] M. Jabbari, R. Bulatova, A. Tok, C. Bahl, E. Mitsoulis and J.H. Hattel, *Mater. Sci. Eng. B*, 2016, **212**, 39.

[28] R.K. Nishihora, P.L. Rachadel, M.G.N. Quadri and D. Hotza, *J. Eur. Ceram. Soc.*, 2018, **38**, 988.

[29] http://www.novabatterysystems.com/lithium-ion.php

[30] K. M. Abraham and Z. J. Jiang, *J. Electrochem. Soc.*, 1996, **143**, 1.

[31] G. Girishkumar, B. Mc. Closkey, A. C. Luntz, S. Swanson and W. Wilcke, *J. Phys. Chem. Lett.*, 2010, **1**, 2193.

[32] S. D. Beattie, D. M. Manolescu and S. L. Blair, *J. Electrochem. Soc.*, 2009, **156,** A44.

[33] H. Cheng and K. Scott, *J. Power Sources*, 2010, **195,** 1370.

[34] J. Read, *J. Electrochem. Soc.*, 2002, **149,** A1190

[35] S. A. Freunberger, Y. Chen, Z. Peng, J. M. Griffin, L. J. Hardwick, F. Barde, P. Novak and P. G. Bruce, *J. Am. Chem. Soc.*, 2011, **133,** 8040.

[36] M. Kotobuki, H. Munakata, K. Kanamura, Y. Sato, and T. Yoshidab, *J. Elecrochem Soc.*, 2010, **157**, A1076.

[37] K. Takada, *Acta. Mater.*, 2013, **61**, 759.

[38] J.B. Goodenough, and K-S. Park, *J. Am. Chem. Soc.*, 2013, **135**, 1167.

[39] Y. Inaguma, C. Liquan, M. Itoh, and T. Nakamura, *Solid State Commun.*, 1993, **86**, 689.

[40] http://www.spring8.or.jp/en/news_publications/press_release/2009/090518/

[41] N. Kamaya, K. Homma, Y. Yamakawa, M. Hirayama, R. Kanno, M. Yonemura, T. Kamiyama, Y. Kato, S. Hama, K. Kawamoto, and A. Mitsui, *Nat. Mater. Lett.*, 2011, **10**, 682.

[42] Y. Kobayashi, M. Tabuchi, and O. Nakamura, *J. Power Sources*, 1997, **68**, 407.

[43] A. Patil, V. Patil, D. Shin, J-W. Choi, D-S. Paik, and S-J. Yoon, *Mater. Research Bull.*, 2008, **43**, 1913.

[44] K. Yamada, N. Sato, T. Fujino, C.G. Lee, I. Uchida, and J.R. Selman, *J. Solid State Electrochem.*, 1999, **3**, 148.

[45] B. Sun, URN: urn:nbn:se:uu:diva-248084, 2015.

Ⅱ. Lithium—oxygen batteries with multi-layered Li^+-selective solid membranes

A. Introduction

Here, we propose an advanced lithium—oxygen battery design based on a multi-layered LSSM with a controlled microstructure using a simple tape-casting process. The thin and dense layer served as a separator and an electrolyte to divide the anode and cathode, and the porous layer mechanically supported the thin layer and provided a space to store the electrolyte when using a liquid electrolyte. Hence, the LOB assembled with the multi-layered LSSM structure presented a low resistance due to the thin layer, superior rate capability, and excellent cycle performance. The use of a multi-layered LSSM structure can be applied to large-scale systems and has the advantage of size controllability.

The multi-layered LSSM was prepared by tape casting using the NASICON-type $Li_{1+x+y}Al_xTi_{2-x}Si_yP_{3-y}O_{12}$ (LATP), which shows a high lithium-ion conductivity and high stability when in contact with organic electrolytes and moisture. In the tape-casting process, an LATP powder slurry was coated, and a dry sheet (green tape) was laminated with layers under different conditions to meet the desired thickness through co-sintering.

B. Experimental

1. Preparation of multi-layered LSSMs

The multi-layered LSSM is manufactured through a tape casting process. $Li_{1+x+y}Al_xTi_{2-x}Si_yP_{3-y}O_{12}$ (LATP) powder (average particle size = 0.4 μm, OHARA Inc., Japan) was first prepared, and BYK111 (dispersant) was mixed with toluene and isopropanol to make a slurry, and then ball milling for 18 h. After adding the binder (polyvinyl butyral) and plasticizer (dioctyl phthalate) to the slurry, followed by ball milling for 18 h. The slurry was degassed with stirring in a vacuum chamber for 3 h. After that, it was coated on the Mylar film and the resulting green tape was dried for 2 h. For the porous tape, polymethyl methacrylate (PMMA, diameter = 5 um), which acts as a pore-forming agent, was added to the mixed slurry before degassing. The green tape was laminated through a warm isostatic press at 1,500 psi and 65 °C for 30 min to form a multi-layered structure. The laminated tape was cut into a size of 28 mm in diameter, heat-treated at 500 °C for 6 h to remove organic components, and then co-sintered at 1,025 °C for 4 h.

2. Material characterizations

The phase and crystal structure of the prepared solid membranes were characterized via X-ray diffraction (XRD) analysis. An automated Rigaku diffractometer (2500 D/MAX, Rigaku) with Cu K_a radiation was used for the XRD measurements. Microstructural analysis was performed using scanning electron microscopy (SEM, Hitachi X‑4900). To examine the sinterability and perform electrical characterization, the LATP powders were pressed into a disk under a pressure of 400 MPa and then sintered at 1,025 ℃ for 4 h in air. The relative density of the sintered sample was estimated using Archimedes' method. To measure the Li^+ conductivity, both sides of the LATP pellet were sputtered with

Au (ion-blocking electrode), and then the AC-impedance spectra were measured in the frequency (f) range of 10^{-1} to 10^{6} Hz with an AC signal amplitude of 5 mV using a Bio-Logic SP-200.

3. Electrochemical experiments

The LOB cell composed of Li metal anode, multilayer LSSM and carbon cathode used a self-made two-compartment cell (Figure 5). The anolyte was 1 M $LiPF_6$ dissolved in a mixed solvent of ethylene carbonate (EC) and ethyl methyl carbonate (EMC) (3:7 by volume), and the catholyte was 1 M Li bis (trifluoromethane-sulfonyl) imide (LiTFSI) in tetraethylene glycol dimethyl ether (TEGDME). The catholyte was directly impregnated into the porous layer, but a porous glass fiber separator was applied to the anode to avoid side reactions between LATP and Li [6]. The cathode was prepared in the form of a fiber having a macroporous structure with a thin carbon nanotube (CNT) (bucky paper) sheet (Figure 6) [7]. For the preparation of CNT bucky paper, CNTs were dispersed in deionized water with Triton X-100 and then sonicated for 1 h. The CNT suspension was filtered through a polytetrafluoroethylene (PTFE) membrane (pore diameter = 0.22 μm), washing with water and methanol to remove residual surfactant under vacuum. The resulting CNT bucky paper was peeled off the PTFE membrane and dried under vacuum. No polymer binder or conductive agent was used. The active area and load of the cathode are 0.785 cm^2 and 1.0 mg cm^{-2}, respectively.

Porous Ni foam is applied to the cathode side for uniform distribution of O_2 gas and efficient current collection. For the comparative study, a commercially available LICGC^{TM} SP-01 membrane (thickness ~180 μm, OHARA Inc., Japan) was used. All cellular components were dried under vacuum at 120 °C. for 12 h and transferred directly to a glove box filled with Ar for cell assembly. The cell was placed in an airtight chamber with controlled pressure and gas flow, and high purity O_2 gas was supplied to the chamber. The galvanostatic discharge-charge profile was measured at a current density of 50 mA g^{-1} (based on the weight of the negative electrode) using a battery tester (WonATech, WBCS3000S). After charging at 50 mA g^{-1} for speed performance testing, the cell was discharged at various current densities of 50 - 1000 mA g^{-1}. Long-term cycling tests were performed with a capacity of 400 mAh g^{-1} at 100 mA g^{-1}. AC impedance measurements were performed at $f = 10^{-2} - 10^{6}$ Hz with an AC signal amplitude of 5mV using Bio-Logic SP-200.

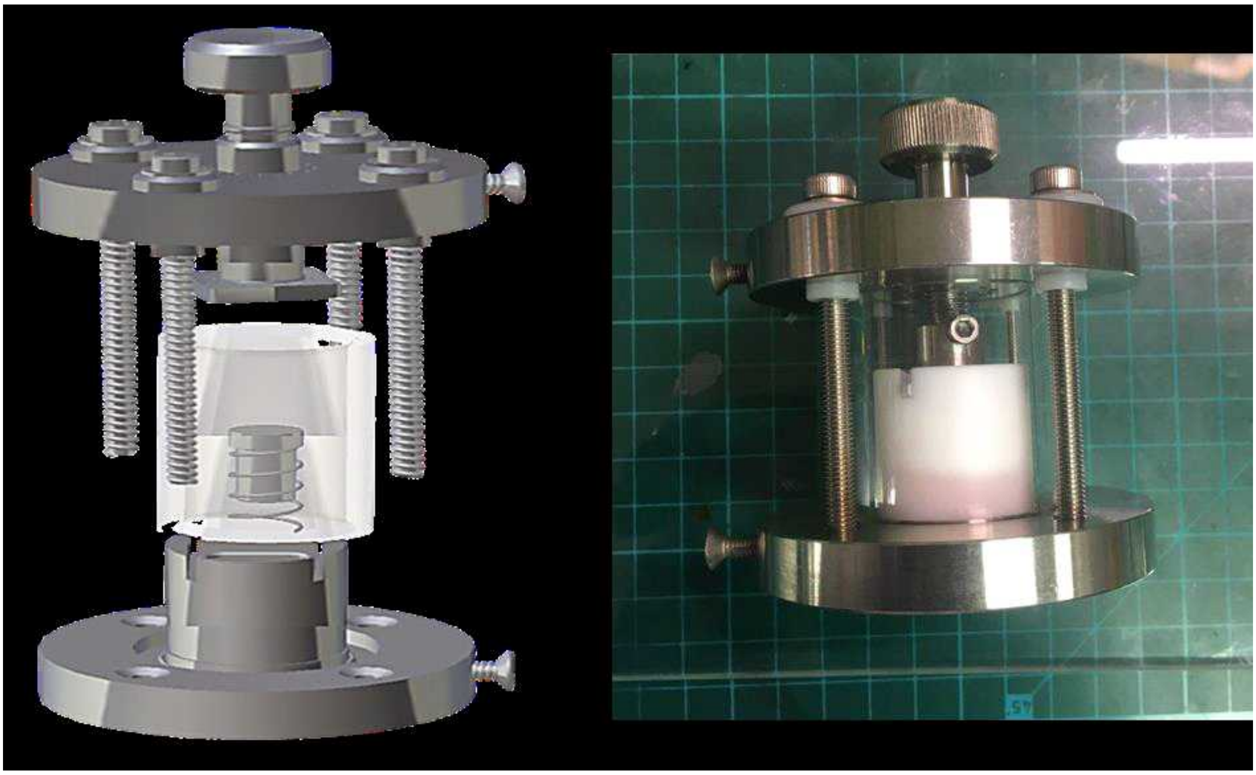

Figure 5. Two-compartment cell used for electrochemical tests.

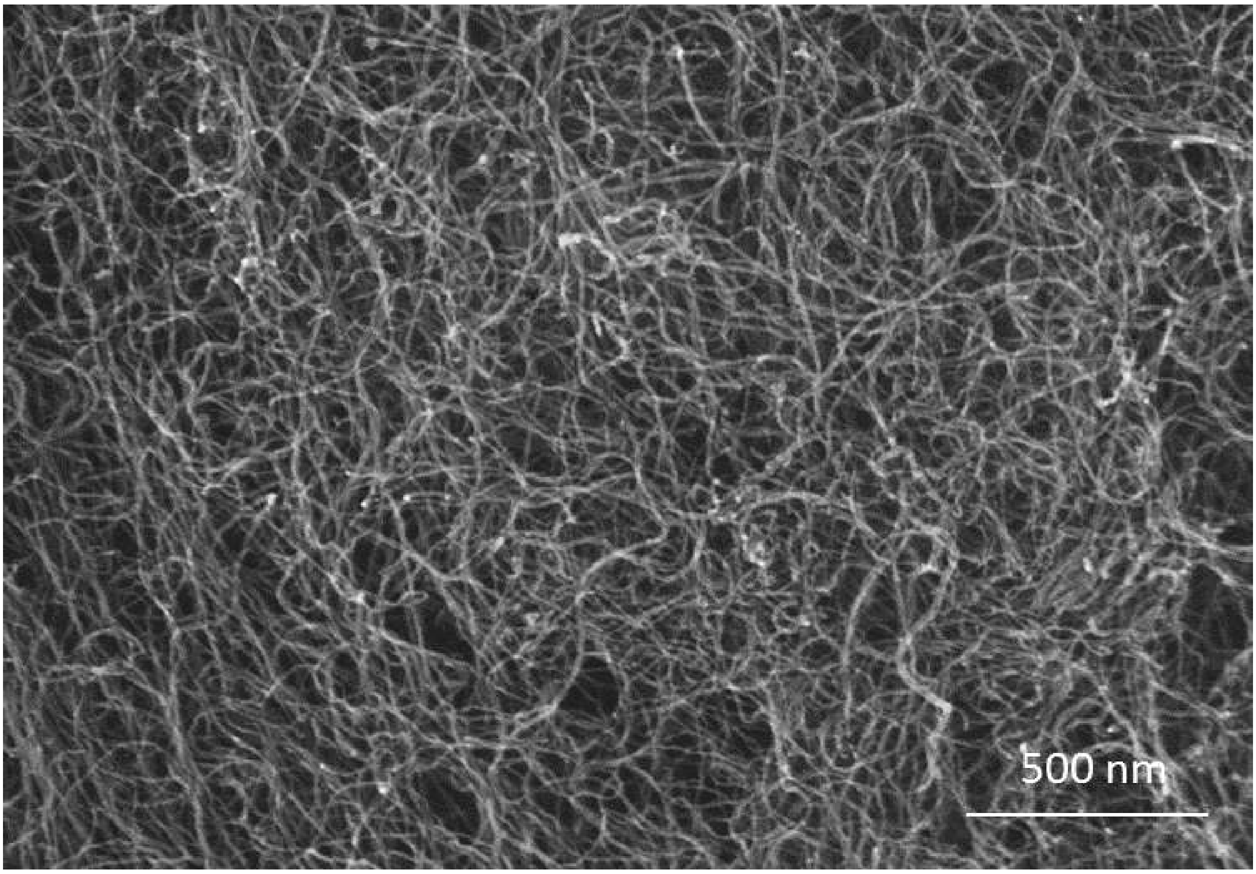

Figure 6. SEM micrograph of CNT buckypaper.

C. Results and Discussion

Figure 7(a) shows an optical image of a green LATP tape with or without 43 wt% PMMA (pore former). The scanning electron microscopy (SEM) image in Figure 7(b) confirms the even dispersion of PMMA particles in the green tape (refer to SEM image of the inserted PMMA). As shown in the inset in Figure 7(c), the multi-layered LSSM was finally obtained through co-sintering at 1,025 °C. Figures 7(c) and 7(d) present a cross section of a multi-layered LSSM and an SEM image of the surface, respectively. Because PMMA acts as a pore former, the outer LSSM layer has microscopic pores. The pores generated by PMMA formed a three-dimensional (3D) porous channel, and the porosity was estimated to be 39% using Archimedes' measurement method. In addition, a cross-sectional SEM photograph showed the presence of a uniformly dense layer without pinholes. In the multi-layered LSSM, the thickness of the porous layer and the dense layer was ~200 and ~35 μm, respectively (Figures 7(c) and 8(a)). Note that no cracking or delamination was present at the interface between the porous and the dense layer after high-temperature simultaneous sintering at 1,025 °C (Figures 7(c) and 8(b)).

The X-ray diffraction pattern for the sintered multi-layered LSSM (Figure 7(e)) shows the characteristic peaks corresponding to the NASICON-type hexagonal $LiTi_2(PO_4)$ three-phase (space group $R\bar{3}c$, JCPDS No. 35-0754). This is in sufficient agreement with the case of the powder sample [5]. This confirms that the sintering process did not cause significant changes in the crystal structure of the multi-layered LSSM.

In a multi-layered structure, the high-density LSSM layer suppresses the diffusion of gas and soluble species, as well as dendritic Li growth, and plays a multifunctional role as a separator between the anode and cathode. In addition, the porous LSSM layer functions as a reservoir for storing liquid electrolytes and supports the dense layer.

The total conductivity of the multi-layered LSSM used in this study is estimated to be $\sim 1.6 \times 10^{-4}$ S cm^{-1} at 25 °C, indicating that it can be successfully operated in LOB (Figure 9). It was also confirmed that liquid cannot penetrate into the dense layer through the colored aqueous solution, as shown in Figure 10.

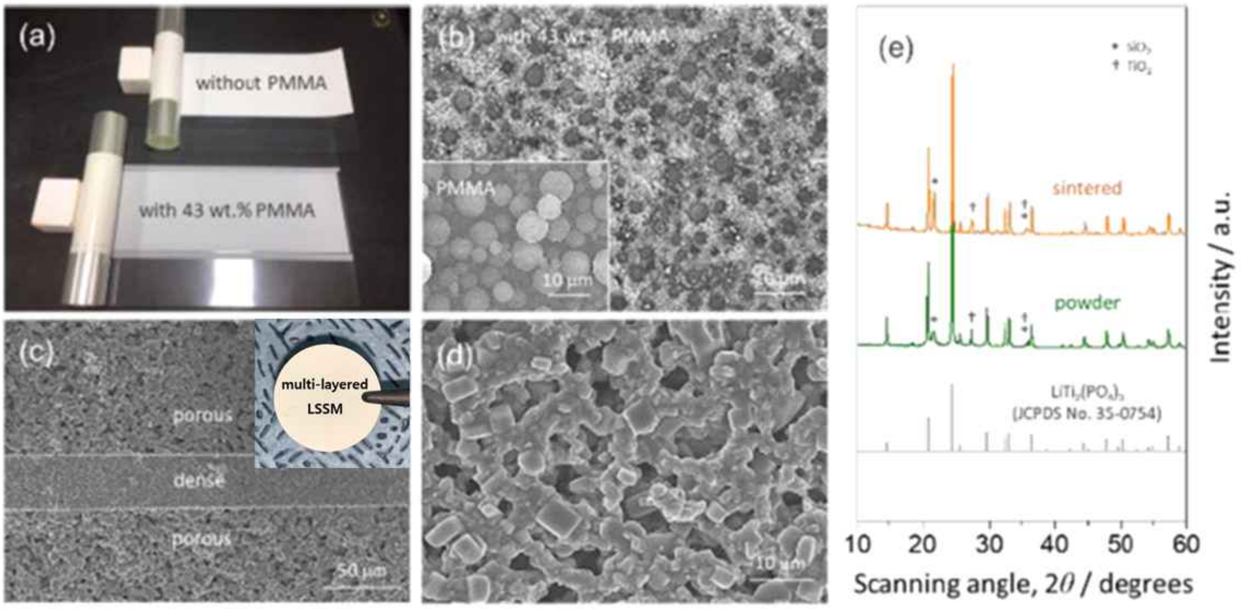

Figure 7. (a) Photograph of the green LATP tapes. (b) SEM images of the PMMA-containing LATP tape. (c) Photograph and cross-sectional SEM image of the sintered multi-layered LSSM. (d) SEM image of the sintered multi-layered LSSM surface (outer porous layer). (e) XRD pattern for the LATP powder and the sintered multi-layered LSSM.

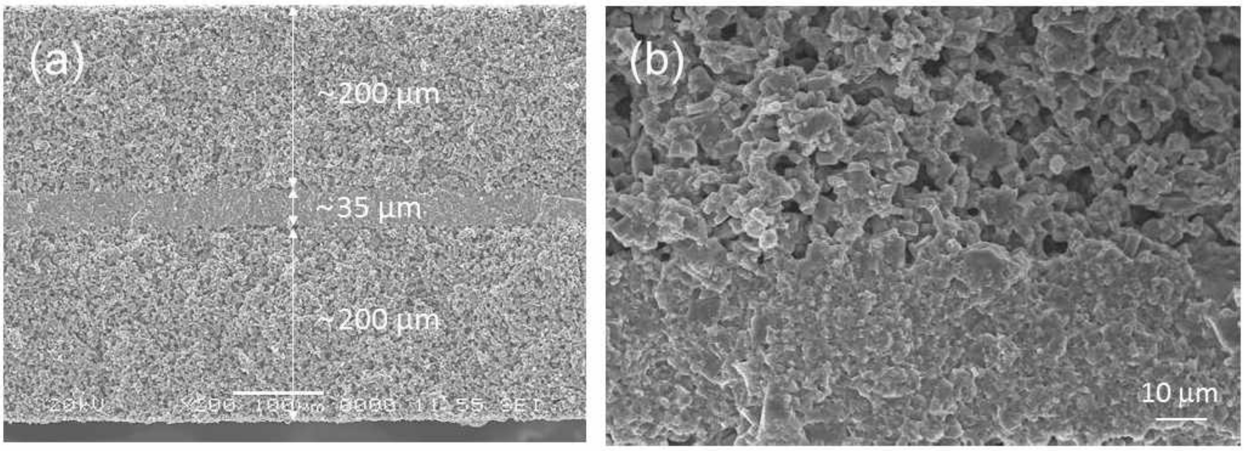

Figure 8. Cross-sectional SEM image of the sintered multi-layered LSSM: (a) low- and (b) high-magnification images.

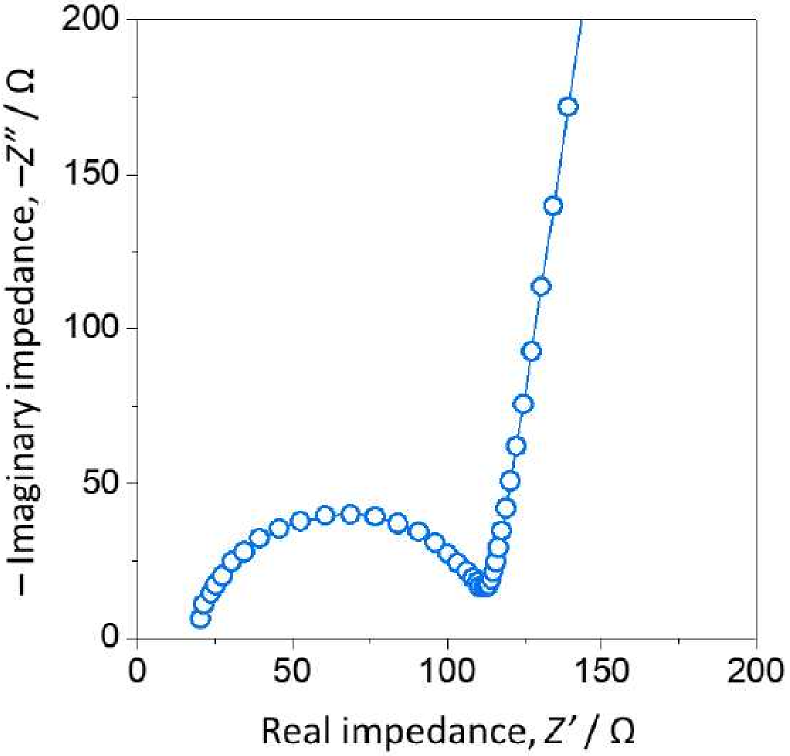

Figure 9. AC-impedance spectrum of the sintered LATP pellet measured using the Au electrodes.

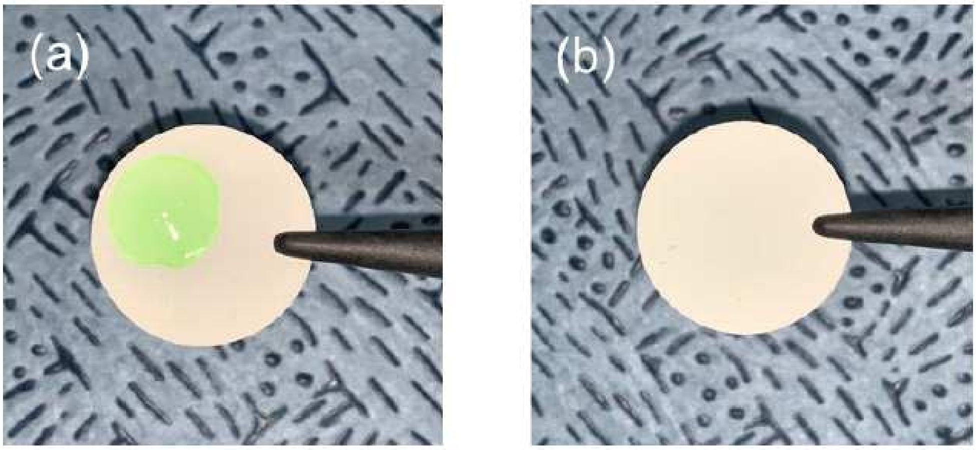

Figure 10. Photographs showing a test of liquid permeation through the multi-layered LSSM. (a) Green-colored liquid was dropped on the one side of the multi-layered LSSM, and then, (b) vacuum was applied on the opposite side. No liquid permeation was observed through the multi-layered LSSM.

To investigate the feasibility of the multi-layered LSSM, a bi-liquid electrolyte LOB cell was designed as follows (Figure 11(a)): Li metal (anode) | Porous LSSM layer | High density LSSM layer | Porous LSSM layer | CNT (cathode). A 1 M LiTFSi in TEGDME was used on the cathode side, and an additional separator was not required because the porous LSSM layer functioned as a reservoir for the liquid electrolyte. However, on the anode side, a glass fiber separator was used to suppress the parasitic reaction to prevent direct contact with Li metal [6]. The anolyte used 1 M $LiPF_6$ in EC/EMC. Figure 11(b) shows a typical discharge–charge curve for an LOB assembled with a multi-layered LSSM. The LOB cell showed a high discharge voltage of 2.7 V *vs.* Li/Li^+. However, at the end of the discharge, it decreased sharply to 2.0 V *vs.* Li/Li^+. The discharge capacity was determined from 50 mAh g^{-1} to 4,717 mAh g^{-1}. Data from existing LOB cells without multi-layered LSSM are also provided for comparison.

As shown in Figure 11(b), the discharge behavior was similar to that of conventional cells without multi-layered LSSM, indicating the successful assembly and excellent operation of LOB cells equipped with multi-layered LSSM. Figure 11(c) shows the AC impedance spectrum of an LOB cell assembled with a multi-layered LSSM. The impedance spectrum consists of two semicircles and a straight line inclined at an angle, which appear in the high-medium frequency range ($f = 10 – 10^6$ Hz) and the low-frequency range ($f < 10$ Hz), respectively. A high–medium frequency semicircle can be associated with Li^+ conduction in multi-layered LSSM (liquid electrolyte impregnation) and interfacial redox reactions (Li_2O_2 formation/decomposition), and straight lines at low frequencies indicate finite-length O_2 diffusion [8,9]. AC impedance data were quantitatively analyzed using the equivalent circuit (Figure 12), and Table 2 presents the results. To differentiate the contribution of lithium-ion conduction in a multi-layered LSSM, AC impedance measurements were performed on a symmetric cell: stainless steel (ion blocking electrode) | Anolyte-dipped separator | Porous LSSM layer | High density LSSM layer | Porous LSSM layer dipped in catholyte | stainless steel (ion-blocking electrode). As shown in Figure 11(d), the impedance spectrum of the symmetric cell of the multi-layered LSSM showed a semicircle at high frequencies (f = 10^4 - 10^6 Hz), and the lines are associated with Li^+ blocking at low frequencies (f < 10^4 Hz). It was estimated to be ~15.5 Ω as the resistance to Li^+ migration within the liquid electrolytes and bulk LATP particles after high-frequency (f ≈ 10^6 Hz) blocking. At f = 10^4 - 10^6 Hz, the semicircle represents the resistance to Li^+ conduction across the grain boundaries of the LATP (~25.6 Ω), accounting for the high-frequency semicircle (~34.2 Ω) in the impedance spectrum for the multi-layered LSSM-based LOB. The impedance of the LOB without the multi-layered LSSM was ~91 Ω at f = 10 - 10^4 Hz (Figure 11(e)), and the semicircle (~112 Ω) observed in the impedance spectrum of the LOB using multi-layered LSSM at the intermediate frequency was interfacial. This is related to the redox reaction.

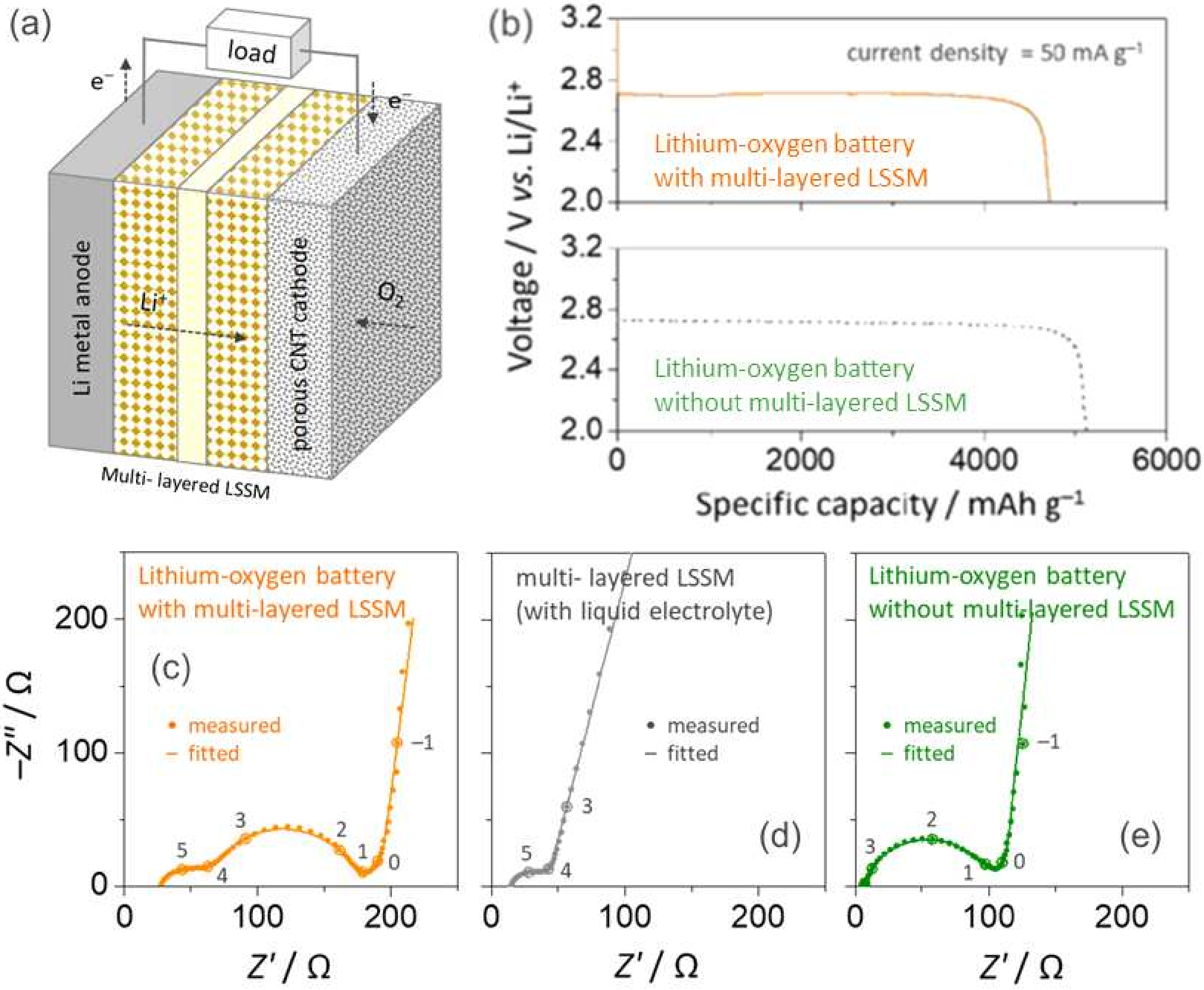

Figure 11. (a) Schematic illustration of a bi-liquid electrolyte LOB cell with the multi-layered LSSM. (b) Galvanostatic discharge profiles of LOBs assembled with and without the multi-layered LSSM. The measurements were performed at a current density of 50 mA g^{-1}. AC-impedance spectra of (c) the LOB assembled with the multi-layered LSSM, (d) the multi-layered LSSM, and (e) the LOB without the multi-layered LSSM. The solid lines represent the results fitted using the equivalent circuits in Figure 12, and the numbers on the open circles indicate logarithmic frequency values.

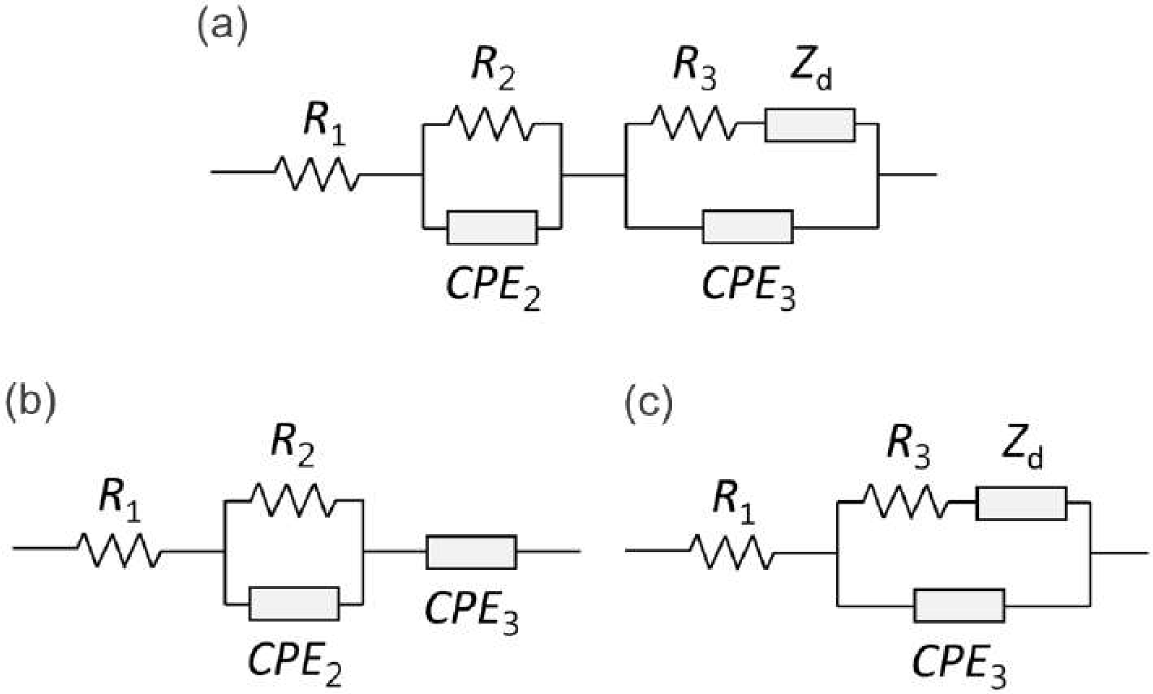

Figure 12. Equivalent circuits used for fitting of the measured impedance data in (a) Figure 11(c), (b) Figure 11(d), and (c) Figure 11(e). R, CPE, and Z_d represent the resistance, constant phase element, and diffusion impedance, respectively.

Table 2. Electrical parameters of the LOB with the multi-layered LSSM (Figure 11(c)), the multi-layered LSSM (Figure 11(d)), and the LOB without the multi-layered LSSM (Figure 11(e)) determined from the CNLS fitting of the impedance spectra to the equivalent circuit (Figure 12).

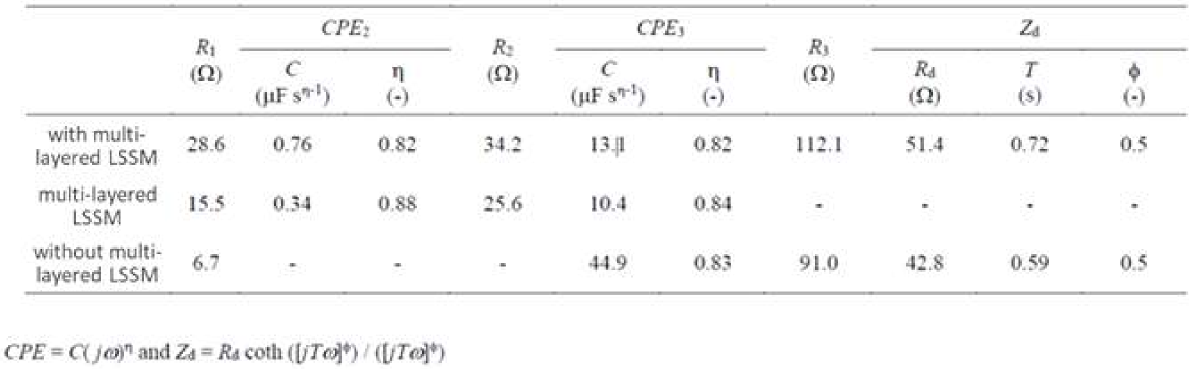

	R_1 (Ω)	CPE_2		R_2 (Ω)	CPE_3		R_3 (Ω)	Z_d		
		C (μF $s^{\eta-1}$)	η (-)		C (μF $s^{\eta-1}$)	η (-)		R_d (Ω)	T (s)	ϕ (-)
with multi-layered LSSM	28.6	0.76	0.82	34.2	13.1	0.82	112.1	51.4	0.72	0.5
multi-layered LSSM	15.5	0.34	0.88	25.6	10.4	0.84	-	-	-	-
without multi-layered LSSM	6.7	-	-	-	44.9	0.83	91.0	42.8	0.59	0.5

$CPE = C(j\omega)^{\eta}$ and $Z_d = R_d \coth([jT\omega]^{\phi}) / ([jT\omega]^{\phi})$

The rate capability was studied by measuring the rectified discharge profile through various current densities ranging from 50 to 1000 mA g^{-1} in an LOB cell with multi-layered LSSM applied at a limited capacity of 400 mAh g^{-1} (Figure 13(a)). The discharge capacity of the LOB was mainly determined by the cathode, and the rate capability of the LOB was evaluated according to the overpotential (η) generated by the discharge reaction [10,11], thus determining the effect of the membrane on the LOB performance. The overpotential (η) was estimated as the difference between the theoretical equilibrium potential (2.96 V *vs.* Li/Li^+) and the measured discharge voltage. For comparison, the same measurement was also made in a cell with a commercially available 180 μm thick LICGC^{TM} membrane. When using LICGC^{TM}, an anolyte separator and a catholyte separator were applied to both sides of the membrane.

As shown in Figure 13(a), the cell voltage rapidly decreased during discharge to reach a steady-state value, but the discharge voltage gradually decreased as the applied current density increased in both cells. At high current densities, LOBs using LICGC^{TM} show ~2.11 V *vs.* Li/Li^+ (η = 0.85 V), while LOBs using multi-layered LSSMs show ~2.20 V *vs.* Li/Li^+ (η = 0.76 V). These results indicate that the cell rate capability is improved owing to the small thickness of the multi-layered LSSM, and the LOB cycling performance operating at a current density of 100 mA g^{-1} is shown in Figure 13(c). The LOB cells were charged and discharged for at least 40 cycles, and no significant change in behavior was observed. This indicated the electrochemical stability as well as the excellent mechanical stability of the multi-layered LSSM.

The presence of LiI, used as the RM in the catholyte, was also demonstrated by a successful charge–discharge operation (Figure 14). Thus far, this is the first study regarding the construction of LOBs using multi-layered LSSM. LOB cells exhibited performance degradation during cycling, as demonstrated by a decrease in discharge terminal voltage and an increase in capacity during constant-voltage charging at 4.3 V *vs.* Li/Li^+ (Figures 13(c) and (d)). The causes of deterioration are carbon instability and parasitic reactions at the cathode due to the electrolyte decomposition, and by-products (e.g., carbonate) are continuously accumulated [12,13].

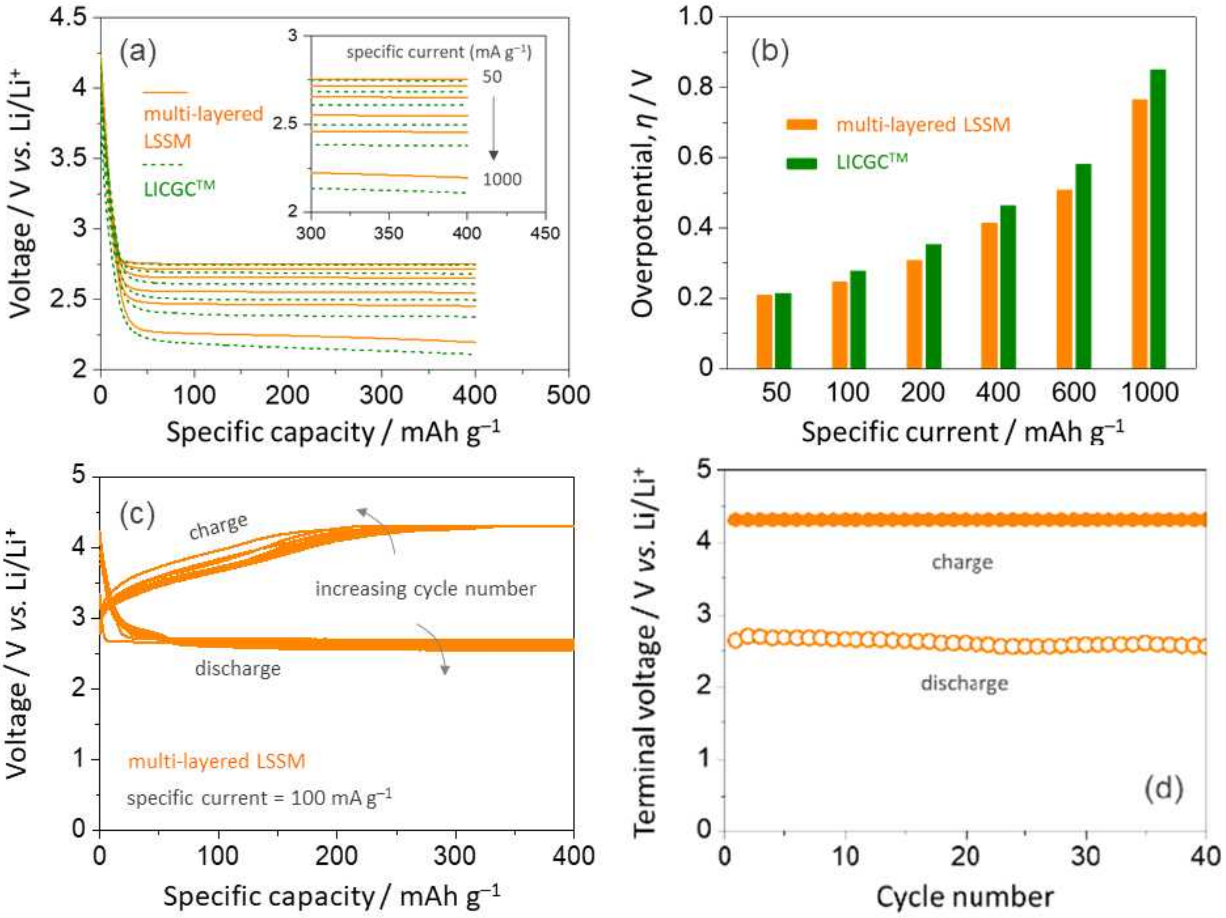

Figure 13. (a) Galvanostatic discharge profiles and (b) cathodic overpotential (η) *vs.* current density plots for LOBs assembled with the multi-layered LSSM and LICGC^{TM}. The cells were discharged at various current densities of 50–1000 mA g^{-1}. (c) Typical discharge‐charge curves for the LOB with the multi-layered LSSM measured during cycling tests at 100 mA g^{-1}. (d) Plots of the terminal discharge and charge voltages *vs.* The cycle number obtained from (c).

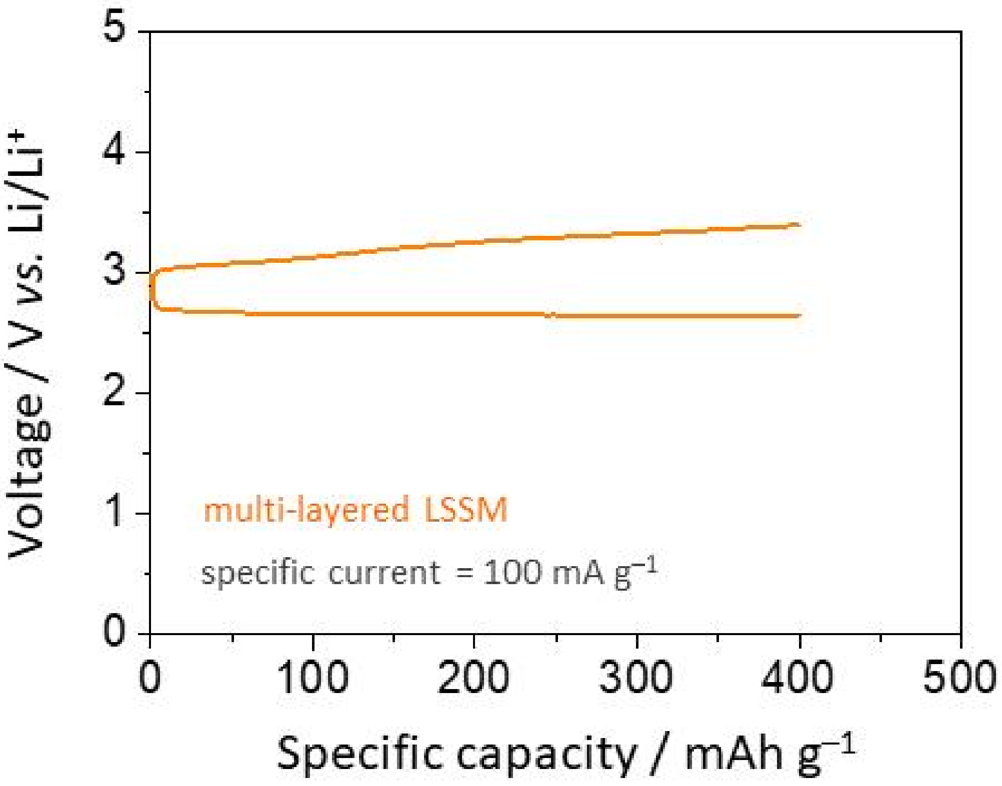

Figure 14. Typical discharge-charge curve of the LOB with the multi-layered LSSM in the presence of LiI as an RM in the catholyte.

D. Conclusions

A stable, stand-alone LATP solid membrane with a multi-layered structure was manufactured through tape casting combined with co-sintering, and then it was applied to a bi-liquid electrolyte LOB cell. The fabricated multi-layered LSSM consists of a porous layer with a mechanical support for the thin layer, a 3D porous channel to store the liquid electrolyte, and a thin dense inner layer that functions as a separator between the electrodes. After co-sintering, no signs of cracking or delamination were observed at the interface between the porous and dense layers. LOB cells assembled with multi-layered LSSM work successfully and exhibit approximately the same discharge behavior as cells with conventional liquid electrolytes. In addition, they exhibit reversible redox behavior and improved rate performance compared to cells that use commercial LICGC^{TM} membranes. The multi-layered architecture does not lose dimensional and mechanical stability and can be easily expanded in size without significant losses.

Reference

[1] Y. Shimonishi, T. Zhang, N. Imanishi, D. Im, D.J. Lee, A. Hirano, Y. Takeda, O. Yamamoto and N. Sammes, *J. Power Sources*, 2011, **196**, 5128.

[2] Y. Sun, *Nano Energy*, 2013, **2**, 801.

[3] P. Zhang, M. Matsui, Y. Takeda, O. Yamamoto and N. Imanishi, *Solid State Ionics*, 2014, **263**, 27.

[4] J.C. Bachman, S. Muy, A. Grimaud, H.-H. Chang, N. Pour, S.F. Lux, O. Paschos, F. Maglia, S. Lupart and P. Lamp, *Chem. Rev.*, 2015, **116**, 140.

[5] S.D. Lee, K.N. Jung, H. Kim, H.S. Shin, S.W. Song, M.S. Park and J.W. Lee, *ChemSusChem*, 2017, **10**, 2175.

[6] P. Hartmann, T. Leichtweiss, M.R. Busche, M. Schneider, M. Reich, J. Sann, P. Adelhelm and J.r. Janek, *J. Phys. Chem. C*, 2013, **117**, 21064.

[7] A. Riaz, K.-N. Jung, W. Chang, S.-B. Lee, T.-H. Lim, S.-J. Park, R.-H. Song, S. Yoon, K.-H. Shin and J.-W. Lee, *Chem. Commun.*, 2013, **49**, 5984.

[8] M. Mirzaeian and P.J. Hall, *J. Power Sources*, 2010, **195**, 6817.

[9] A. Riaz, K.-N. Jung, W. Chang, K.-H. Shin and J.-W. Lee, *ACS Appl. Mater. Interfaces*, 2014, **6**, 17815.

[10] K.-N. Jung, J.-H. Jung, W.B. Im, S. Yoon, K.-H. Shin and J.-W. Lee, *ACS Appl. Mater. Interfaces*, 2013, **5**, 9902.

[11] Z.D. Yang, X.Y. Yang, T. Liu, Z.W. Chang, Y.B. Yin, X.B. Zhang, J.M. Yan and Q. Jiang, *Small*, 2018, **14**, 1800590.

[12] B.D. McCloskey, A. Speidel, R. Scheffler, D. Miller, V. Viswanathan, J. Hummelshøj, J. Nørskov and A. Luntz, *J. Phys. Chem. Lett.*, 2012, **3**, 997.

[13] J. Lu, K.C. Lau, Y.-K. Sun, L.A. Curtiss and K. Amine, *J. Electrochem. Soc.*, 2015, **162**, A2439.

Ⅲ. Solid-state lithium—oxygen batteries based on multi-layered Li^+-selective solid membranes

A. Introduction

In this study, we designed a novel solid-state LOB integrated with a dense LATP-electrolyte layer with a 39% porous LATP-cathode support. Hence, we propose and prepare a multi-layered LSSM@CNT@Au with the following key components. (i) An LSSM protects Li metal anodes from side reactions with impurity species and reactants (e.g., O_2, H_2O, and CO_2) that diffuse from the outside. (ii) A thin LSSM layer (50 mm thick) with relatively high mechanical properties can prevent dendrite growth from occurring on Li metal anodes during repeated cycling. (iii) A porous LSSM cathode expands the TPBs by depositing an electron conductor onto the porous structure of the LSSM, forming a three-dimensional pathway for the entire cathode to lithium ions, electrons, and oxygen. (iv) Au nanoparticles coated on carbon nanotubes have received extensive attention for reduction owing to their high mechanical stability, reasonable electron conductivity, and improved catalytic activity. Our results provide evidence of the enhanced performance in the discharge capacity and the life cycle of these solid-state LOBs when operating in pure air. This unique design with an integrated cathode structure is very safe and shows a positive potential for superior solid-state LOBs.

B. Experimental

1. Preparation of multi-layered LSSM@CNT cathodes

The CNT cathodes were deposited onto the multi-layered LSSM porous layer scaffold via a chemical vapor deposition (CVD) process. First, Cobalt (II) nitrate hexahydrate ($Co(NO_3)_2 \cdot 6H_2O$, 1.455 g) were dissolved in DI water (10 ml) and stirred for 1 h. After that, the solutions were slowly drop casted injected into the multi-layered LSSM porous layer and then dried at 90 °C for 30 min. The dried samples and 0.5 g Dicyandiamide (DCDA, 99%) were placed into a covered crucible in a tube furnace, which were heated at 400 °C for 3 h, then at another controlled temperature 800 °C for 1 h under a N_2 atmosphere. Finally, a uniform CNT deposited with a loading of 1.0 mg cm^{-2} (projected area) was obtained.

2. Preparation of multi-layered LSSM@CNT@Au cathodes

Au was coated onto the surface of CNTs using the Ion sputter coater (GSEM, G20) technique. The multi-layered LSSM@CNT@Au was coated with a gold layer (~10 nm thick). The chamber was firstly evacuated to vacuum environment of a base pressure of 2.0×10^{-1} Torr. The sputtering time was 120 s and operate ion current was 10 mA.

3. Material characterizations

The morphologies and micro structures of the synthesized materials were examined by SEM (Hitachi, S4800), Raman spectroscopy (Thermo Scientific, Nicolet Almega XR). A FESEM Hitachi S-4800 operating at 10 kV was used to observe morphologies of processed samples. For post-test SEM characterization, the samples were cleaned with 1,2-dimethoxyethane (DME, Sigma-Aldrich) to remove residual substances. Transmission electron microscopy (TEM) images were obtained by operating a high-resolution Hitachi HF-3300 TEM system. The samples were dispersed in ethanol, sonicated and dripped onto the holey carbon-coated Cu grids. The surface chemistry was investigated by XPS (Thermo Scientific, ESCALAB 250Xi). Spectral background was optimized using a combination of Shirley and Linear functions simultaneously with spectral fitting. X-ray photoelectron spectroscopy (XPS, Thermo Scientific, ESCALAB 250Xi) were used to analyses the formation and decomposition of cathode products during discharge and charge processes.

4. Electrochemical experiments

The electrochemical performance of LOBs was evaluated by building 2032 coin cells in an Ar-filled glovebox with $O_2 < 0.1$ ppm and $H_2O < 0.1$ ppm. The liquid electrolyte was 1 M Li bis(trifluoromethane-sulfonyl)imide (LiTFSI) in tetraethylene glycol dimethyl ether (TEGDME). The values of current density and specific capacity of the oxygen cathodes relied on the total weight of carbon cathode. All compounds of the cell were also dried under vacuum at 120 °C for 24 h before being transferred into the glovebox. Galvanostatic discharging and charging tests were operated on a battery test system (WonATech, WBCS3000L32) at room temperature after 7 h rest. For a comparative study, a cell was assembled using a freestanding CNT buckypaper. Porous Ni foam was placed on the cathode side to enable uniform distribution of O_2 gas as well as efficient current collection. The cell was placed in a gas-tight chamber with a controlled gas flow rate and pressure, and high-purity O_2 gas was supplied to the chamber. Long-term cycling tests were performed with a 400 mA h g^{-1} capacity at 50 mA g^{-1}.

C. Result and Discussion

The concept of the LOBs with the multi-layered LSSM@CNT@Au design is shown in Figure 15(a). With the porous density double structure, lithium ions react with oxygen in the porous layer of the solid electrolyte along the interconnected structure of the dense layer and form lithium peroxide during discharge to fill the porous pores. With the multi-layered LSSM, the plating and/or stripping of the lithium metal and the formation and/or decomposition of the discharge product lithium peroxide are limited to a solid-state framework, preventing battery short circuits due to lithium dendrite growth and volume expansion of the cathode. CNTs formed into the pores and uniformly coated Au nanoparticles helped with the formation of film-like lithium peroxide and minimized the formation of by-products, such as Li_2CO_3. The multi-layered LSSM electrolyte LOB was assembled without the TEGDME-based organic electrolyte on the cathode side. During the charge–discharge process, the reversible reactions of O_2 reduction to form Li_2O_2 and its reverse oxidation to Li^+ and O_2 occur at three-phase interfaces. The equation is $2Li^+ + O_2 + 2e^- = Li_2O_2$, with a standard electrode potential of 2.96 V *vs.* Li/Li^+ [1]. Figure 15(b) presents a schematic illustration of the synthesis process for the multi-layered LSSM@CNT@Au air electrode.

The multi-layered LSSM was designed via an expandable tape casting method, and the resulting samples were cut to fit the coin cell size (Figure 16(a)). On the cathode side of the porous layer, the cobalt solution was pre-coated into the porous layer by repeated infusion (Figure 16(b)). In the following step, the as-prepared multi-layered LSSM@Co was then pyrolyzed by heating to 400 °C for 3 h under N_2 gas flow. Subsequently, the cathode was grown with uniform, 3D carbon nanotubes (CNTs) by DCDA powder at 800 °C for 1 h in pure N_2 gas. Carbon nanotubes (CNTs) are uniformly coated into the porous layer structure, introducing the electronic conductivity of the porous layer within the framework (Figure 16(c)). Then, a multi-layered LSSM@CNT@Au was prepared by magnetron sputtering using a gold template. The typical loading mass of the CNTs on multi-layered

LSSM@CNT@Au was ~1 mg cm^{-2}. The characterization of the LATP based multi-layered LSSM electrolyte is shown in Figure 17. Figure 17(a) presents the full-scale scanning electron microscopy (SEM) image of the seamless multi-layered LSSM structure, in which the bottom dense layer serves as the electrolyte (~30 mm thick), while the top porous layer functions as support (~250 mm thick and 39% porous). Continuous pores can be observed from the surface of the porous layer (Figures 17(b) and (c)). The porous layer provides sufficient space for lithium and oxygen to react to achieve high energy density battery systems. The dense layer has no pinholes and blocks the connection between the anode and cathode, preventing the growth of dendrites and diffusion of impurity species (Figure 17(d)). The boundary between the dense layer and the porous layer confirms a well-connected structure with no gaps, showing one pore in the porous cathode support and indicating a clear borderline. All layers are made of the same material, LATP, and are seamlessly connected through high-temperature sintering without the conventional potential barrier, resulting in a small resistance of the Li^+ transport and a small interfacial resistance between the electrolyte and the cathode.

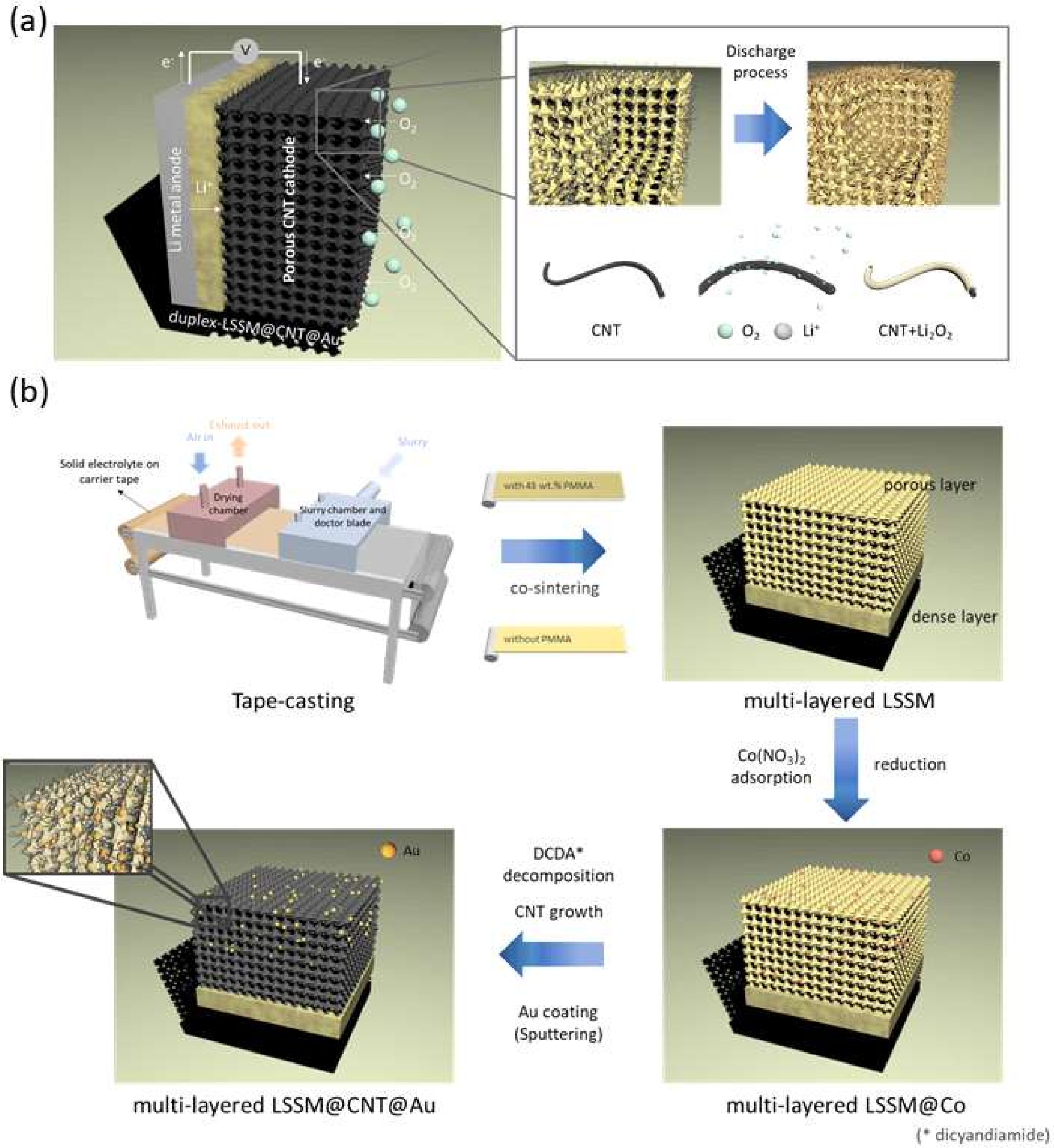

Figure 15. (a) Schematic representation of the proposed solid-state LOB using Li Anode, multi-layered LSSM, and an air electrode composed of multi-layered LSSM@CNT@Au. (b) Schematic diagram illustrating synthesis process of the multi-layered LSSM@CNT@Au structure.

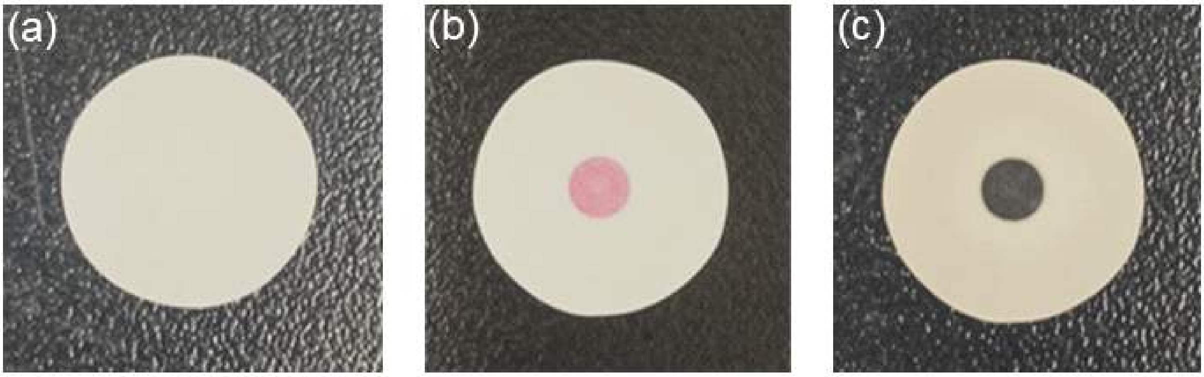

multi-layered LSSM

multi-layered LSSM@Co

multi-layered LSSM@CNT

Figure 16. Digital photographs of (a) green multi-layered LSSM, (b) multi-layered LSSM@Co, and (c) multi-layered LSSM@CNT.

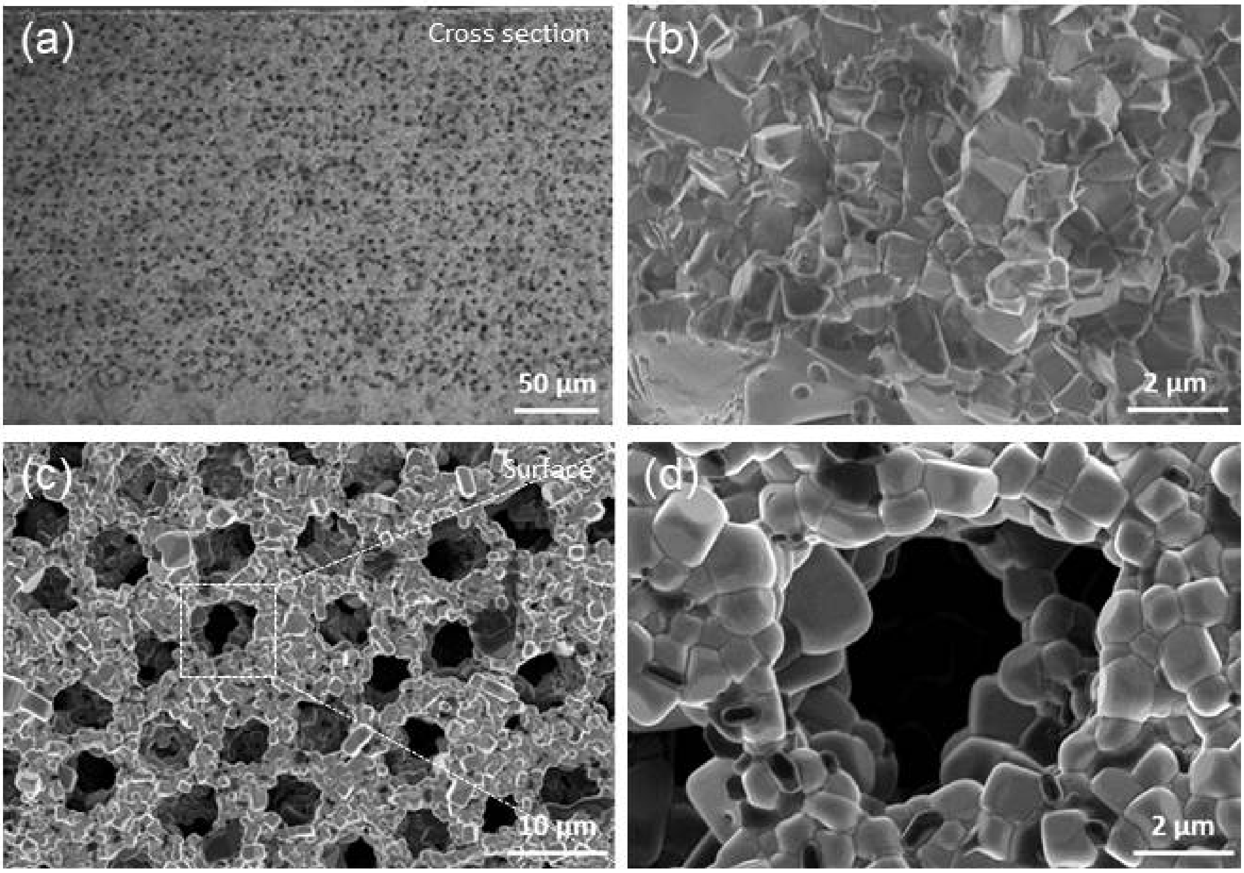

Figure 17. SEM images of the (a) Low magnification cross sectional of the multi-layered LSSM solid electrolyte layer. (b) Cross sectional SEM image of the dense layer indicating no pores. (c) the surface of the multi-layered LSSM layer, and (b) a typical pore in the porous layer.

The SEM images of CNTs grown over the Co nanoparticles by thermal CVD of N_2 at 800 °C are shown in Figure 18. Cobalt particles are uniformly distributed and maintain intimate contact (Figure 18(a)). Figure 18(b) shows the air electrode on the multi-layered LSSM@CNT by the cross-sectional SEM images. The scanning electron microscopy (SEM) image of the multi-layered LSSM@CNT (Figure 18(c)) shows that the CNTs were uniformly grown on the porous LSSM. This regulates the ionic transport channels and increases the contact surface area between the ionic conductor and the electronic conductor. As shown in Figure 18(d), after the deposition of CNTs, the air electrode maintains its porous structure and sufficient contact with the multi-layered LSSM pellet. The high-magnification SEM image and tilt image demonstrate that a large number of CNTs are linked to each other to construct 3D porous networks (Figure 18(e)). Figure 18(f) presents the SEM images and energy-dispersive X-ray spectroscopy (EDX) results from the multi-layered LSSM@CNT@Au air electrode. The corresponding EDX elemental mapping (Figure 19) demonstrates that C, N, Co, and Au atoms are homogeneously distributed throughout the electrode. Both phosphorus and titanium, as components of the multi-layered LSSM, are uniformly distributed over the entire structure, and the structural characteristics do not change after the CNT@Au process.

Transmission electron microscopy (TEM) images (Figures 20(a) - (d)) indicate that the cobalt metal nanoparticles were successfully encapsulated in bamboo-like carbon nanotubes with an average diameter of 100 - 200 nm. Cobalt metal nanoparticles were observed at the head end of CNTs in the size range of 30 - 50 nm. The typical bamboo-like structure in CNTs indicates the formation of a carbon network under a nitrogen atmosphere [2]. As shown in Figure 20(b), lattice fringes with d spacing of 0.34 nm of CNT were consistent with a (001) planar spacing, suggesting that the (001) plane of CNT is sufficiently grown [3]. Graphitic carbon structures are formed in the catalytic graphitization behavior of Co NPs [4]. Co NPs are wrapped in the graphitic carbon layers, which benefits the stability of the ORR electrocatalysis regardless of whether an alkaline or acidic electrolyte is used. The cobalt NPs maintained their size with negligible sintering under high annealing temperatures owing to the protection of the graphitic carbon shell around the Co

NPs [5]. Figure 21 presents the TEM elemental mapping of the multi-layered LSSM@CNT@Au after the Au deposit on the cathode. Elemental mapping indicated that CNT@Au is mainly composed of C, Co, and Au, which coexist and are highly dispersed in the walls of the CNTs. Raman spectroscopy was used to characterize the carbon crystallinity. As shown in Figure 22(a), there are two remarkable peaks at approximately 1360 and 1576 cm^{-1} in the Raman spectra. Two typical bands were observed, in which the D band (~1360 cm^{-1}) represents the disordered graphite structure and the G band (~1576 cm^{-1}) represents the crystalline graphite carbon. The intensity ratio of the D and G bands (ID/IG) was used to estimate the disorder in the materials [6]. The higher ID/IG ratio implies more defects in the N-CNTs. The ID/IG values were estimated to be 0.9 for multi-layered LSSM@CNT, indicating that multi-layered LSSM@CNT has an improved graphitization degree and better electrical conduction [7,8]. It is known that a large surface area increases the number of active sites as well as the adsorption of oxygen molecules on the surface [9]. To improve the performance of LOBs, not only the high Co/N content of the multi-layered LSSM@CNT cathode is required but also the high density of the active sites. As depicted in Figure 22(b), the high-resolution N 1s spectrum indicated the presence of four types of nitrogen species: pyridinic-N at ~398.6 ± 0.2 eV, graphitic-N at ~401.1 ± 0.3 eV, pyrrolic-N at ~400.5 ± 0.3 eV, and pyridinic oxide at ~404.3 eV [10]. According to a previous study [11,12], there is a graphitic-N, which accelerates the kinetics of the four-electron process at the ORR, and pyridinic N, which can promote O_2 reduction by increasing the p state density, current, and spin density of C atoms close to the Fermi level. The functional groups on the carbon surface induced by N doping improve the cycle stability by enhancing the chemical affinity [13,14]. Therefore, the high pyridinic- and graphite-N contents of multi-layered LSSM@CNT is important because it promotes the adsorption and reduction reactions of oxygen. As shown in Figure 22(c), the oxidation state of Au in CNT@Au was determined by X-ray photoelectron spectroscopy. The XPS spectrum of the CNT@Au complex shows a doublet with binding energies of Au 4f$^{7/2}$ (84.0 eV) and Au 4f$^{5/2}$ (87.7 eV), which is a typical value indicating that Au NPs sufficiently formed on the CNT sidewalls.

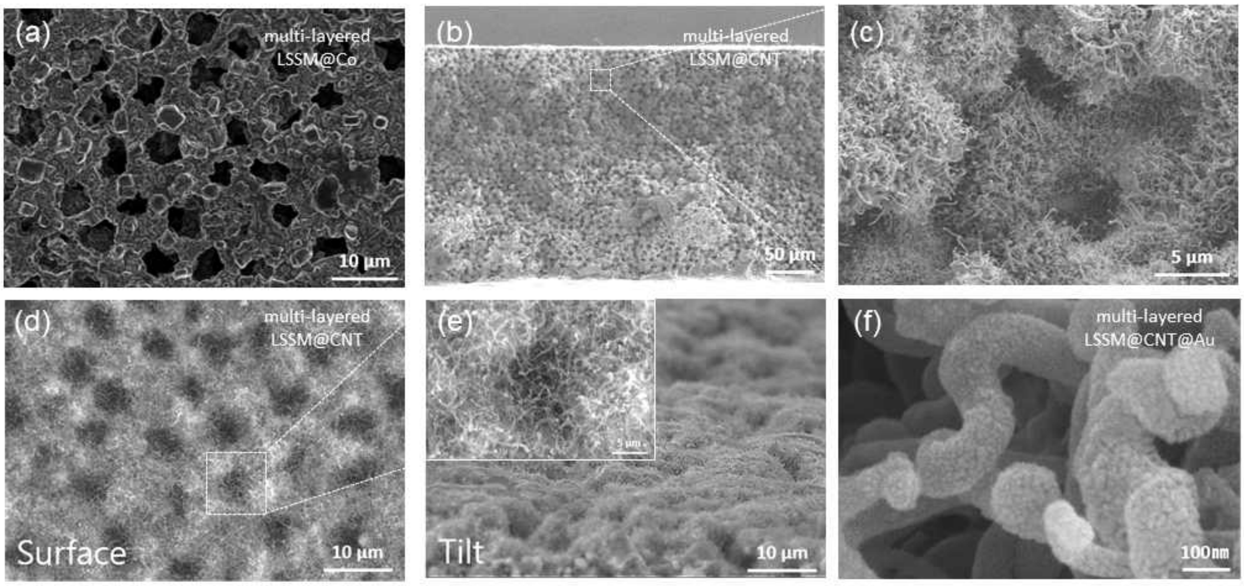

Figure 18. (a) Co nanoparticles distributed on the multi-layered LSSM, (b) Low-magnification and (c) high-magnification SEM images of the cross sectional of multi-layered LSSM@CNTs. (d) Low-magnification SEM images of the surface of multi-layered LSSM@CNTs. (e) SEM cross-section images taken at a tilt. The inset shows high-magnification SEM images of the surface of multi-layered LSSM@CNTs. (f) High-magnification SEM images of the multi-layered LSSM@CNT@Au.

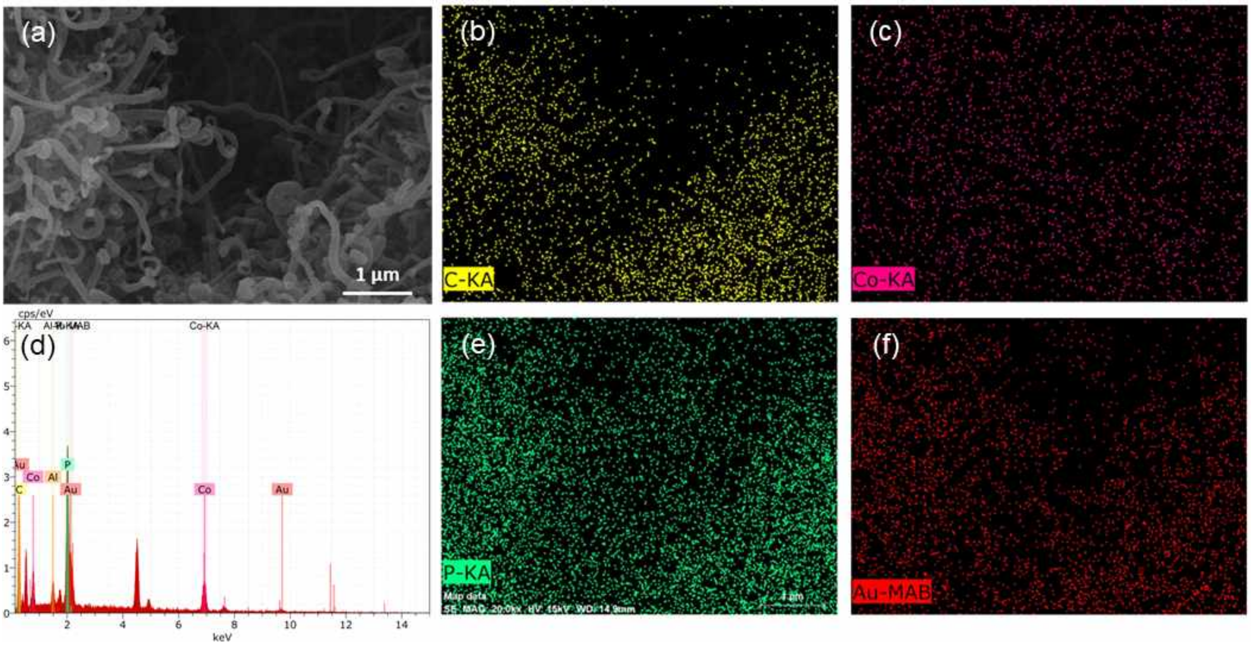

Figure 19. The high-magnification SEM micrographs (a) and energy dispersive X-ray spectroscopy (EDS) spectrum (d) of the multi-layered LSSM@CNT@Au and the corresponding elemental distribution maps of C, Co, P, and Au (b - f).

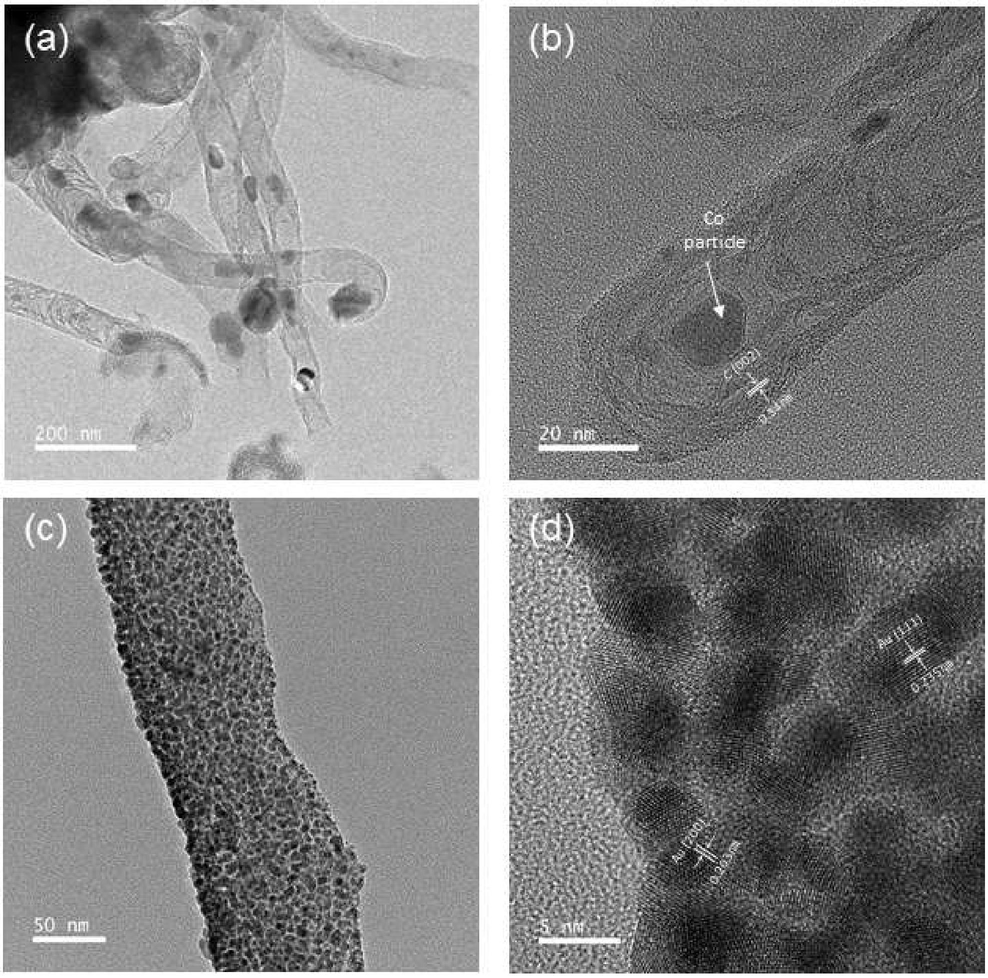

Figure 20. (a) High magnification TEM image of CNT. (b) High magnification TEM image of Co nanoparticle on Co@CNT. (c-d) Low and magnification TEM image of multi-layered LSSM@CNT@Au. Au was uniformly deposited of the multi-layered LSSM@CNT.

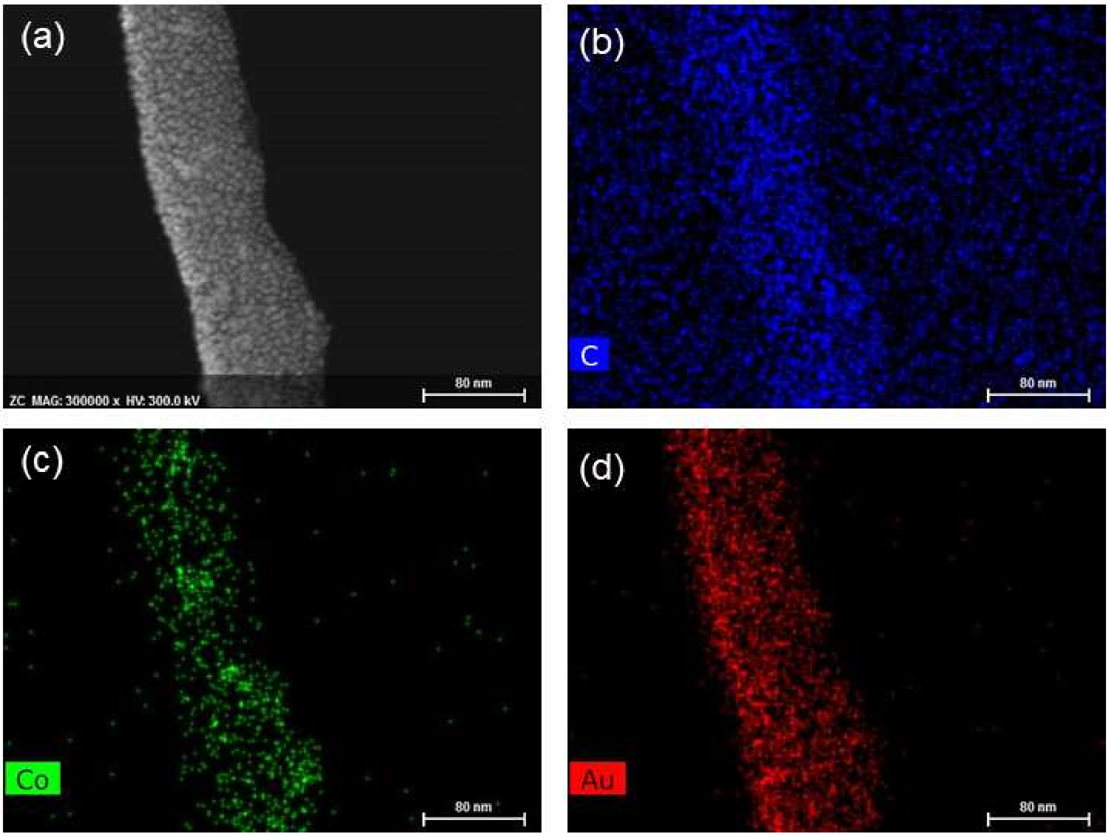

Figure 21. (a) TEM image and EDS elemental mapping results of multi-layered LSSM@CNT@Au composites for C (b), Co (c), and Au (d).

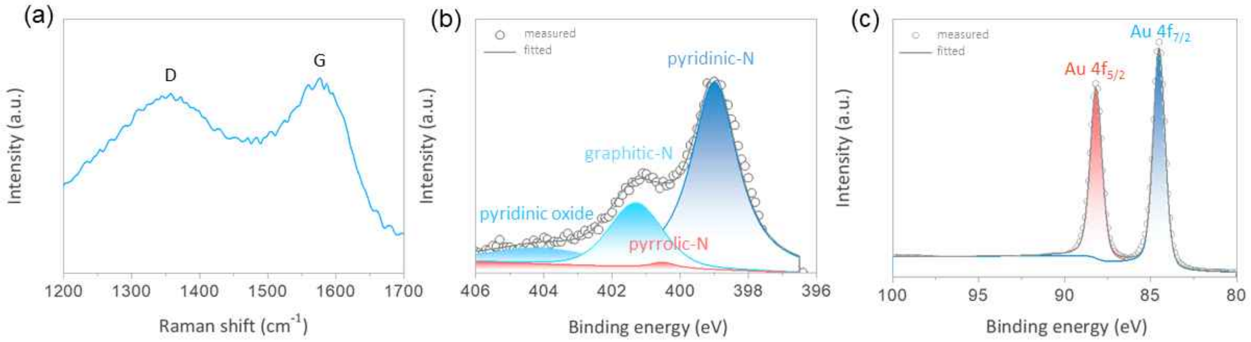

Figure 22. (a) Raman spectra of multi-layered LSSM@CNT. XPS survey spectra and high-resolution scans of (b) N 1s, and (c) Au 4f electrons of multi-layered LSSM@CNT@Au, respectively.

The multi-layered LSSM was prepared on a pouch cell with a small hole in diameter. The multi-layered LSSM fully covered the lithium metal. A closed, homemade chamber was filled with pure oxygen/moisture. After exposure to moist air for a few days, the changes in the lithium metal inside the chamber were recorded. The results show that the multi-layered LSSM protected the Li foil, which remained shinning after 3 days, while the control sample turned gray after 1 d (Figure 23(a)). Inspired by the protective effect of the multi-layered LSSM, Li|Li symmetric cells cycled in the O_2 atmosphere were fabricated. Figure 23(b) compares the galvanostatic charge‐discharge performance of the symmetric cells with the multi-layered LSSM and without the multi-layered LSSM. Asymmetric Li/without multi-layered LSSM/Li cell was also prepared and tested for comparison. The symmetric cells were charged and discharged with a limited capacity of 0.5 mAh cm^{-2} at room temperature under the current density of 0.2 mA cm^{-2}. The Li/multi-layered LSSM/Li cell exhibited a small polarization (< 0.25 V) and an unexpected stable cycling of 1100 h. The multi-layered LSSM-based cell showed low voltage hysteresis (overpotential between Li deposition and dissolution) for more than > 1100 h without cell failure, which is apparently superior to the performance of the cell without the multi-layered LSSM. This clearly demonstrates that the cycling stability is improved substantially with the protection of the multi-layered LSSM. The enlarged voltage profiles present that the Li/without multi-layered LSSM/Li symmetric cells display a large polarization (i.e., ~1.0 V), and a small overpotential peak can be observed at the beginning of each cycle. In contrast, the multi-layered LSSM battery shows smooth voltage curves. According to Chen et al. [15], this small peak is due to the formation of lithium dendrites. However, no similar small peak can be observed in the curve of the multi-layered LSSM symmetric cell, which demonstrates that the existence of the multi-layered LSSM suppresses the growth of lithium dendrites. Figure 24 presents SEM and XPS after discharging and charging the sample. Discharge products with a film-like structure are formed on the surface of the air electrode, and after charging, the discharge product can be observed to be nearly completely decomposed. The ability of the sample to decompose the discharge products was further confirmed through XPS testing. After testing, it was found at 54.5 eV, which is the peak of Li_2O_2 corresponding to the discharge product. After 30 cycles, CNT paper (with LE) and multi-layered LSSM@CNT@Au (without LE) were compared to characterize the product of the air electrode. The results after the test showed a significant accumulation of Li_2CO_3 (Figure 25), which consequently caused electrode passivation and LOB failure using CNT paper earlier due to incomplete decomposition of discharge products, as well as parasitic reactions at the cathode. However, the multi-layered LSSM@CNT@Au had a stable surface at 30 cycles, which is also shown in the XPS results. When the cycle is completely finished, Li_2CO_3, a discharge product that has not been decomposed due to exposure to air, is considered to accumulate on the cathode surface similar to LOBs using CNT paper and is terminated.

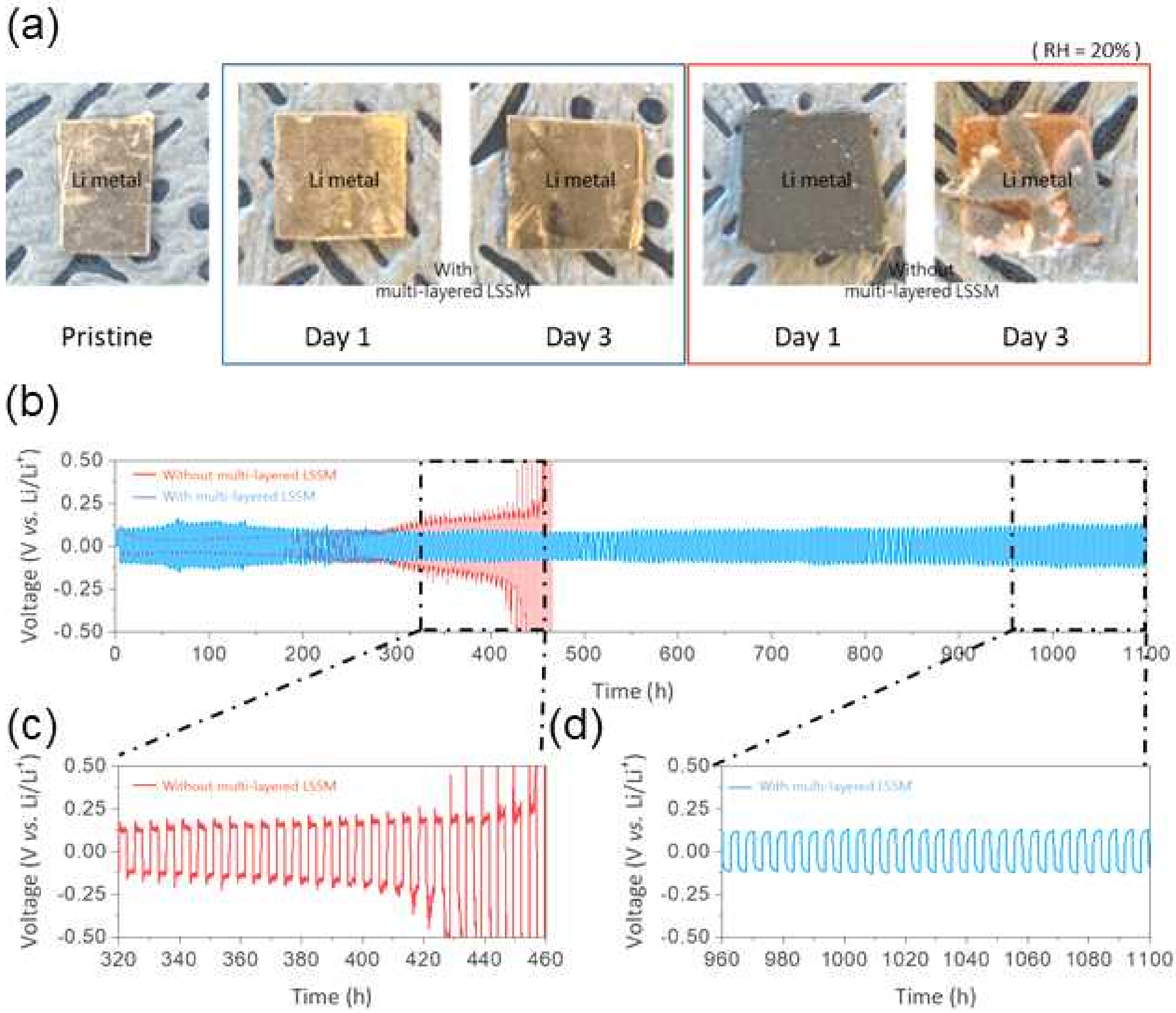

Figure 23. (a) Photographs of Li metal with multi-layered LSSM and without multi-layered LSSM exposed to air with a relative humidity of 20 % for 3 days. (b) Symmetric cell cycling performance comparison between with(blue) and without(red) multi-layered LSSM under 0.2 mA cm^{-2}. Areal capacity was fixed at 0.5 mA h cm^{-2}. Voltage profiles of (c) without multi-layered LSSM and (d) with multi-layered LSSM at the selected cycles.

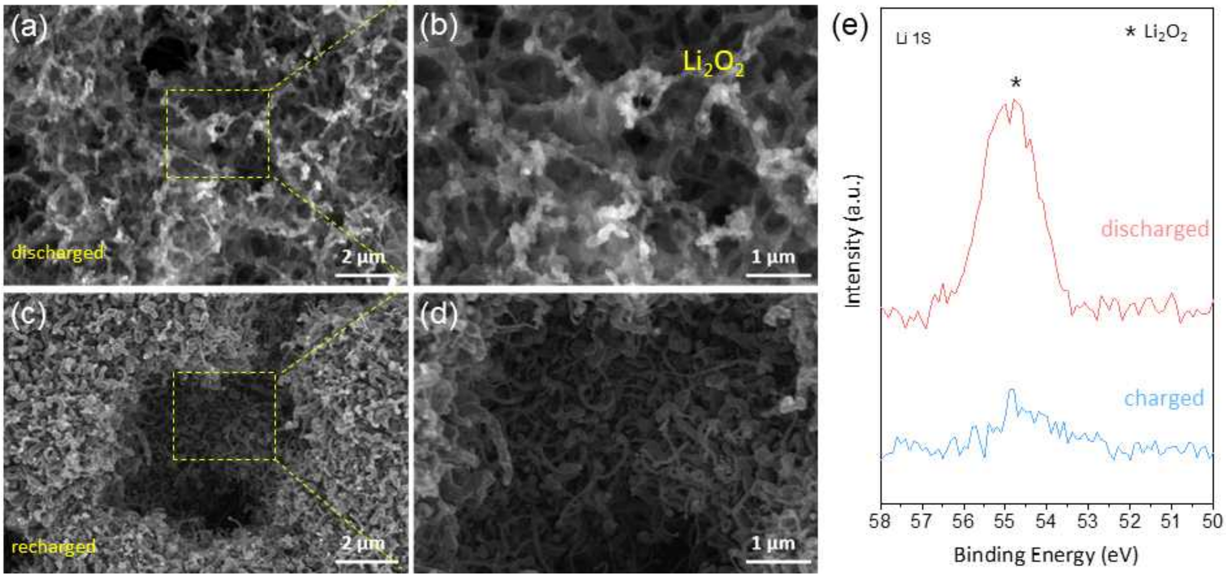

Figure 24. SEM images of the discharge product (a–b) after a full discharge to 2.0 V *vs.* Li/Li$^+$. (c - d) SEM images of the recharged multi-layered LSSM@CNT cathode at a current density of 50 mA g^{-1}. (e) XPS survey spectra of the discharged and charged cathodes.

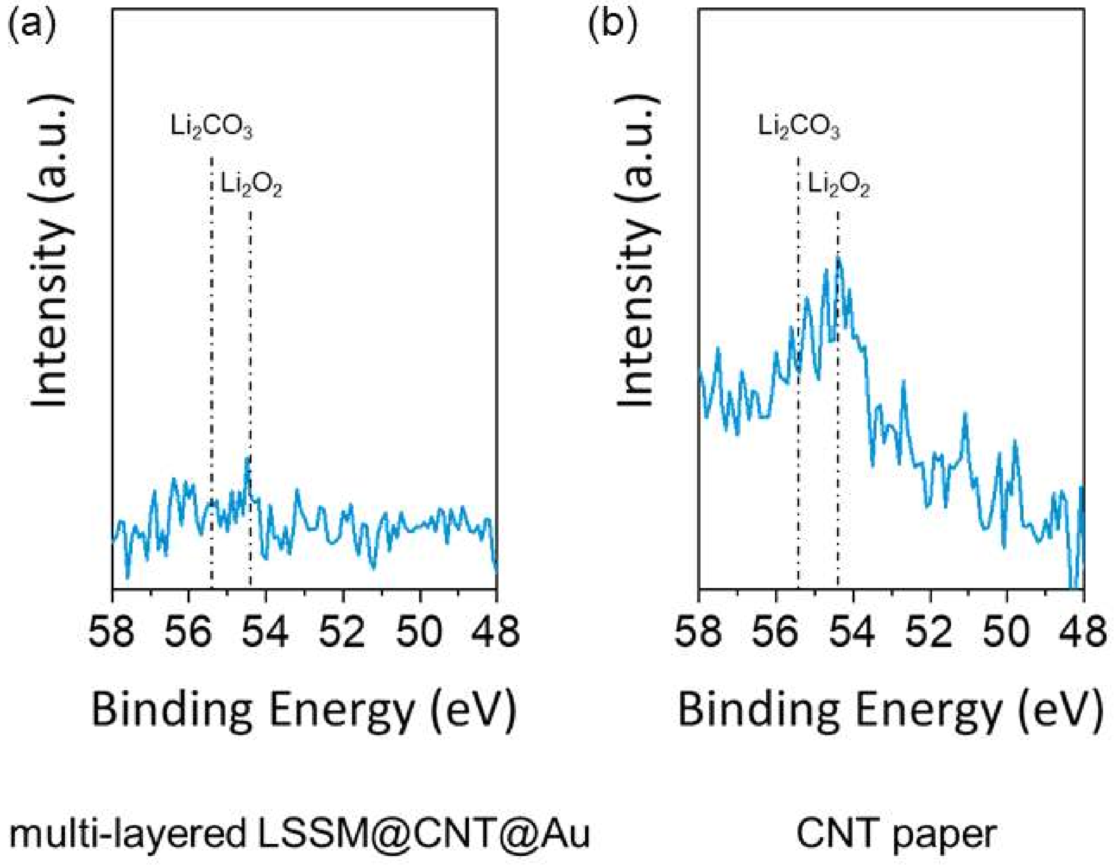

Figure 25. Li 1s XPS spectra of the recharged multi-layered LSSM@CNT@Au and CNT paper electrodes after cycling test in O_2.

As a proof-of-concept, the electrochemical properties of multi-layered LSSM@CNT@Au were then analyzed in LOBs. Meanwhile, CNT paper is also employed as electrodes in LOBs for comparison. The cathode side was tested with a solid-state structure, and a liquid electrolyte was used on the anode side to ensure contact between the Li metal and the solid electrolyte. All the results of the electrochemical measurements were normalized based on the loading weight of the cathode. Figure 26(a) shows the full potential range discharge performances of LOBs with multi-layered LSSM@CNT@Au (without LE), multi-layered LSSM@CNT (without LE), CNT paper (with LE), and CNT paper (without LE). The current density was set to 50 mA g^{-1} and the cut-off voltage was set to 1.8 V. The specific capacity of the air-cathode in the multi-layered LSSM@CNT@Au cell was 3500 mAh g^{-1}, which is approximately 1.2 times lower than that of the control cell (4400 mAh g-1). However, as shown in Figure 26(b), the battery with multi-layered LSSM@CNT@Au exhibits significantly enhanced cycling performance. Conversely, the CNT paper (with LE) cells have a rapid increase in overpotential and rapidly end the life cycle. These results indicate that multi-layered LSSM@CNT@Au cathodes possess superior electrochemical performances in LOBs, which may be derived from the synergy of the following advantageous factors. (i) The self-standing and binder-free structure of multi-layered LSSM@CNT is the advantage of enabling rapid oxygen and electrolyte diffusion and providing sufficient pores to the house discharged product. (ii) In situ growth of active CNTs provides a strong interconnection between the active material and the electrode without gaps, improves the catalytic activity, and improves the stability of the cathode. (iii) The multi-layered LSSM@CNT@Au has exceptional ORR activity. Their synergistic effect could lead to the efficient formation and decomposition of the discharge product Li_2O_2. In addition, the well-integrated tunnels for both electrons and ions of the composite air electrode were important for the improved performance [16-20]. Figure 26(c) presents the discharge‐charge profiles for LOBs with multi-layered LSSM@CNT and CNT paper cathodes at a current density of 50 mA g^{-1} with a fixed capacity of 400 mAh g^{-1}. The cell was successfully discharged and charged. The multi-layered LSSM@CNT@Au cathode can achieve

100 cycles with a discharge terminal of > 1.8 V. In contrast, CNT paper cathodes can only achieve 44 cycles. The multi-walled carbon nanotubes from multi-layered LSSM@CNT@Au were found to function as a continuous electron conduction path based on better crystallinity and excellent catalytic properties, indicating that they are relatively stable. As shown in Figure 26(d), during discharging, the battery with multilayered LSSM@CNT@Au had a plateau of approximately 2.7 V, and its discharging overpotential was clearly smaller than that with CNT paper (with LE), which is apparently related to the sufficient ORR catalytic behavior of multi-layered LSSM@CNT@Au. The improved electrode performance of the multi-layered LSSM@CNT@Au compared to that of CNT without Au is presumably due to its improved electrical conductivity owing to the deposition of Au NPs. The center of the discharge and charge voltage was approximately 3.1 V, which is consistent with the theoretical potential for the formation and decomposition of Li_2O_2 [21].

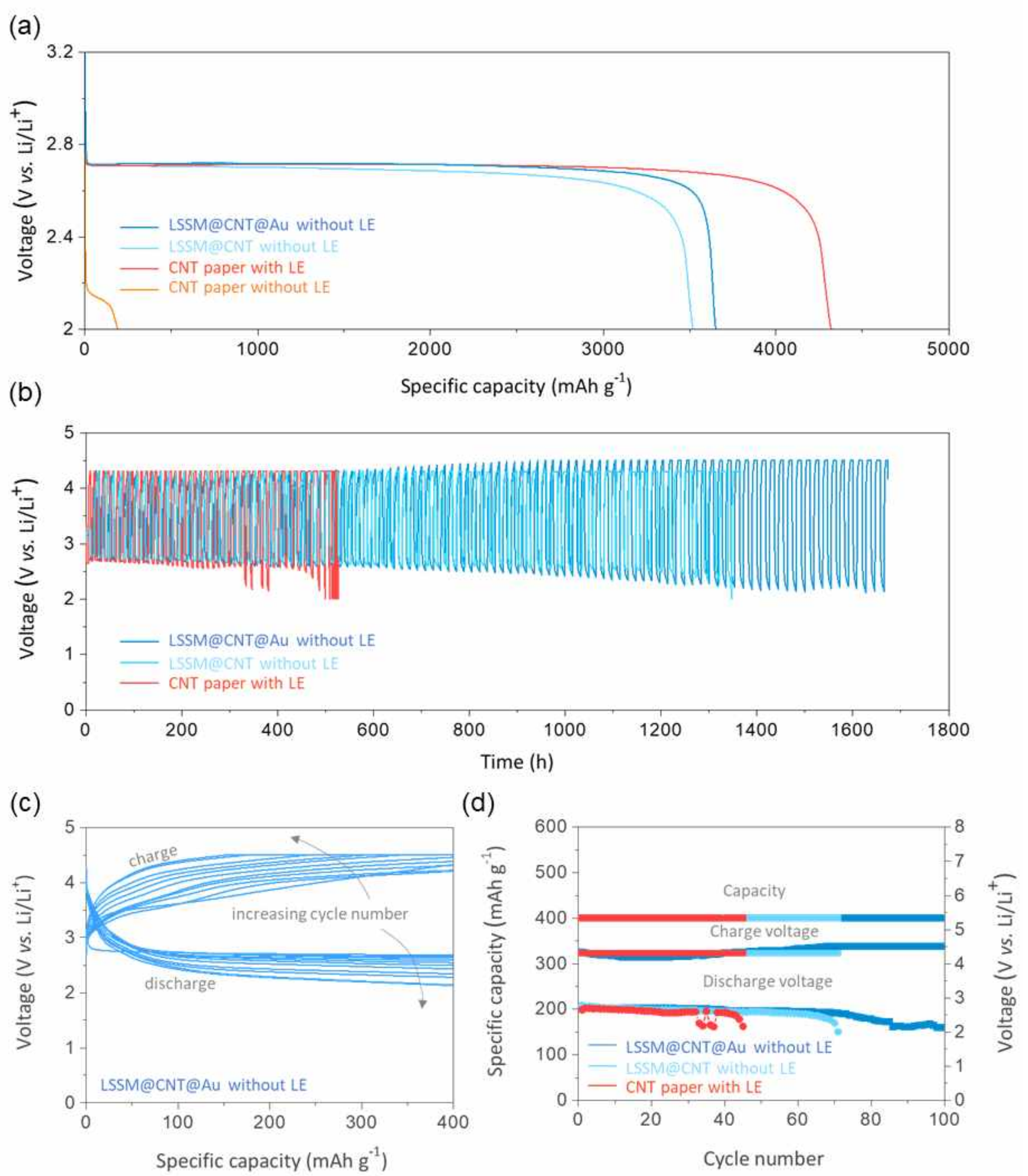

Figure 26. (a) Galvanostatic discharge profiles of LOBs assembled with multi-layered LSSM@CNT@Au (without LE), with multi-layered LSSM@CNT (without LE), with CNT paper (without LE), and with CNT paper (with LE). The measurements were performed at a current density of 50 mA g^{-1}. (b) Cycling performances of LOBs with multi-layered LSSM@CNT@Au (without LE) and with CNT paper (with LE) measured at current density of 50 mA g^{-1}. (c) Discharge-charge profiles of LOB with multi-layered LSSM@CNT@Au (without LE) at selected cycles. (d) Plots of discharge capacity versus cycle number for LOBs with multi-layered LSSM@CNT@Au (without LE) and with CNT paper (with LE).

D. Conclusions

A multi-layered LSSM structure was fabricated by the tape-casting method, and CNT growth was simply performed using a furnace. In addition, Au particle coating was easily produced through sputtering. The manufactured multi-layered LSSM@CNT@Au has a 3D channel, provides a space to accommodate discharge products, and generates high ORR and OER reactions. After the CVD process, the structural properties of LATP did not change, and the porosity remained constant. By applying a multi-layered LSSM to the LOB, lithium metal could be suppressed from side reactions by external species, and dendritic lithium was suppressed. In addition, the discharge behavior was similar to that of the previously used CNT paper applied cell but presented excellent performance in the life cycle, decomposition, and formation of discharge products. The produced cathodic porous membrane showed excellent performance without using a liquid electrolyte, and it is expected to open a solution to the battery market, such as electric vehicles in the future.

Reference

[1] B. D. Mccloskey , D. S. Bethune , R. M. Shelby , T. Mori , R. Scheffler , A. Speidel , M. Sherwood and A. C. Luntz, *J. Phys. Chem. Lett.*, 2012, **3**, 3043.

[2] Yue J, Gu X, Jiang X, Chen L, Wang N, Yang J, Ma X., *Electrochim Acta.,* 2015, **182**, 676-681.

[3] F. Li, S. G. Chou, W. Ren, J. A. Gardecki, G. R. Harrison, A. K. Swan, M. S. Unlu, B. B. Goldberg, H.-M. Cheng and M. S. Dresselhaus, *J. Mater. Res.*, 2003, **18**, 1251-1258.

[4] Y.Z. Chen, C. Wang, Z.Y. Wu, Y. Xiong, Q. Xu, S.H. Yu, H.L. Jiang, *Adv. Mater. (Weinheim, Ger.).*, 2015, **27**, 5010-5016.

[5] J. Masa, W. Xia, M. Muhler, W. Schuhmann, *Angew. Chem. Int. Ed.*, 2015, **54**, 10102-10120.

[6] M. A. Pimenta, G. Dresselhaus, M. S. Dresselhaus, L. A. Cancado, A. Jorio, R. Saito, *Phys. Chem. Chem. Phys.*, 2007, **9**, 1276-1290.

[7] Close M.Q. Wang, C. Ye, S.J. Bao, Z.Y. Chen, Y.N. Yu, Y. Zhang, M.W. Xu, *Chem. Commun.*, 2016, **52**, 12992-12995.

[8] G. Panomsuwan, N. Saito, T. Ishizaki, *ACS Appl. Mater. Interfaces*, 2016, **8**, 6962-6971.

[9] K. Gong, F. Du, Z. Xia, M. Durstock, L. Dai, *Science*, 2009, **323**, 760-764.

[10] Y.N. Hou, Z. Zhao, Z. Yu, Y. Tang, X. Wang, J. Qiu, *Chem. Commun.*, 2017, **53**, 7840-7843.

[11] X. Cui, S. Yang, X. Yan, J. Leng, S. Shuang, P.M. Ajayan, Z. Zhang, *Adv. Funct. Mater.*, 2016, **26**, 5708-5717.

[12] J. Liu, P. Song, W. Xu, *Carbon*, 2017, **115**, 763-772.

[13] Y. C. Qiu, W. F. Li, W. Zhao, G. Z. Li, Y. Hou, M. N. Liu, L. S. Zhou, F. M. Ye, H. F. Li, Z. H. Wei, S. H. Yang, W. H. Duan, Y. F. Ye, J. H. Guo, Y. G. Zhang, *Nano Lett.* 2014, **14**, 4821-4827.

[14] J. X. Song, Z. X. Yu, M. L. Gordin, D. H. Wang, *Nano Lett.*, 2016, **16**, 864-870.

[15] Chen KH, Wood KN, Kazyak E, Lepage WS, Davis AL, Sanchez AJ, Dasgupta NP, *J. Mater. Chem. A*, 2017, **5**, 11671-11681.

[16] Xueping Zhang, Xiaowei Mu, Sixie Yang, Pengfei Wang, Shaohua Guo, Min Han, Ping He, Haoshen Zhou., *Energy & Environmental Materials*, 2018, **1**, 61-74.

[17] Chu-Shu Yang, Kang-Ning Gao, Xiao-Ping Zhang, Zhuang Sun, Tao Zhang., *Rare Metals*, 2018, **37**, 459-472.

[18] Yijie Liu, Ping He, Haoshen Zhou., *Advanced Energy Materials*, 2018, **8**, 1701602.

[19] Waruni Jayawardana, Christopher L. Carr, Dongxue Zhao, Eric H. Majzoub., *Journal of The Electrochemical Society*, 2018, **165**, A2824-A2832.

[20] Wang Zhang, Yue Shen, Dan Sun, Zhimei Huang, Yunhui Huang., *Advanced Energy Materials*, 2017, **7**, 1602938.

[21] R. Padbury and X. Zhang, *J. Power Sources*, 2011, **196**, 4436-4444.

감사의 글

대학원이라는 진로를 결정하였을 때가 엊그제인 것 같은데 벌써 대학원 졸업을 바라보게 되었습니다. 대학원 진학 후, 많은 걱정이 있었으나 석사 과정을 무사히 끝마칠 수 있도록 도와주신 모든 분들에게 먼저 감사의 인사를 올립니다. 2년이라는 시간이 그렇게 긴 시간은 아니지만 많은 것들에 대해서 배울 수 있었으며 편협한 사고방식에 변화를 끌어낼 수 있는 좋은 시간이었습니다. 이제 그 마지막을 바라보며 이 석사 논문을 마무리 짓기위해 마침표를 찍으려 하니 시원섭섭한 마음이 가득합니다.

제가 대학원이라는 진로에 대해서 마음을 갖게 해주시며 영원한 멘토로 남게 될 저의 지도교수님이신 이종원 교수님, 정말 감사하다는 말씀을 올립니다. 조선대학교에 오시며 에너지라는 분야에 대해서 새롭게 눈을 뜨게 해주셨으며, 창의적인 관점에서 미래를 대비할 수 있도록 학업뿐만 아니라 지혜까지 아낌없이 주셔서 너무나도 감사드립니다. 또한, 저의 논문 심사를 맡아주셨으며 학부 때부터 훌륭한 강의를 해주셨던 강현철 교수님, 이종국 교수님, 신동찬 교수님 감사합니다.

조선대학교에서 있었던 우리 에너지 소재 연구실 사람들 (영수, 형준, 종혁, 은서), 대학원에 들어오면서 실험실을 처음부터 꾸려야 했던 우리 모습을 생각하면.... 정말 수고했다. 아무것도 모르며 시작했지만, 교수님께 배우며 부족한 부분이 있으면 서로에게 물어보며 채워나가고 힘들면 술도 한 잔씩 하면서 미운 정 고운 정 많이 들었지... 졸업하고 나서도 언제나 생각날 꺼야. 그리고, DGIST에 있는 EEMI (우영, 홍림), 비록 1 년 정도의 시간을 보냈지만, 아침부터 저녁까지 부딪히며 살았던 동생들이자 친구들이던 너네도 고마웠어. 타지에서 올라와 아무것도 모르지만 낯가리지 않으며 친근하게 대해주고 언제나 문제가 있으면 같이 고민해주고 같이 해결해주려고 하는 모습들 고마웠어.. 덕분에 석사 생활 마지막까지 재밌었고 더 열심히 할 수 있었다고 생각하고 졸업해서도 한 번씩 보러 찾아올게.

마지막으로 우리 가족들, 무슨 대학원을 가느냐부터 시작해서 많은 걱정을 나 못지않게 많이 했겠지만 그래도 믿고 맡겨줘서 고맙고, 언제나 사랑합니다. 이제 곧 사회초년생으로 나아가게 되는데 지금까지 받았던 사랑 다 갚도록 하겠습니다. 언제나 아프지 말고 항상 건강하길 바랍니다.